

A Test of Lepton Universality Using the $\tau^- \rightarrow e^- \bar{\nu}_e \nu_\tau$ Decay

by

Ian T. Lawson
B.Sc., University of New Brunswick, 1993

A Thesis Submitted in Partial Fulfillment of the
Requirements for the Degree of

MASTER OF SCIENCE

in the Department of Physics and Astronomy

We accept this thesis as conforming
to the required standard

Dr. R.J. Sobie, Supervisor (Department of Physics and Astronomy)

Dr. R.K. Keeler, Co-supervisor (Department of Physics and Astronomy)

Dr. G. Beer, Departmental Member (Department of Physics and Astronomy)

Dr. P. Wan, Outside Member (Department of Chemistry)

Dr. M. Vetterli, External Examiner (TRIUMF)

© Ian Timothy Lawson, 1995
University of Victoria

All rights reserved. Thesis may not be reproduced in whole or in part, by photocopying or other means, without the permission of the author.

Supervisor: Dr. R.J. Sobie

Co-supervisor: Dr. R.K. Keeler

ABSTRACT

The electronic branching ratio of the tau lepton has been determined from data collected by the OPAL detector at LEP from 1991 to 1994. A total of 29738 $\tau^- \rightarrow e^- \bar{\nu}_e \nu_\tau$ candidates were found from a sample of 83474 $e^+e^- \rightarrow \tau^+\tau^-$ candidates. Using efficiency and background estimates determined from a study of Monte Carlo events and control samples of data, the branching ratio $B(\tau^- \rightarrow e^- \bar{\nu}_e \nu_\tau) = 0.1778 \pm 0.0009 \pm 0.0011$ was obtained, where the first error is statistical and the second is systematic. The electronic branching ratio was then used to test the assumption of the universality of charged current leptonic couplings in the standard model.

Examiners:

Dr. R.J. Sobie, Supervisor (Department of Physics and Astronomy)

Dr. R.K. Keeler, Co-supervisor (Department of Physics and Astronomy)

Dr. G. Beer, Departmental Member (Department of Physics and Astronomy)

Dr. P. Wan, Outside Member (Department of Chemistry)

Dr. M. Vetterli, External Examiner (TRIUMF)

Contents

Abstract	ii
Table of Contents	iii
List of Tables	vi
List of Figures	viii
Acknowledgements	xiii
1 Introduction	1
2 Theory	5
2.1 Standard Model	5
2.2 The Decay Width	8
2.2.1 Higher Order Corrections	11
2.2.2 The Total Width	12
2.3 Lepton Universality	12
2.4 The $\tau^- \rightarrow e^- \bar{\nu}_e \nu_\tau$ Branching Ratio Formulation	13
3 The OPAL Experiment	15
3.1 The LEP Collider	15
3.2 The OPAL Detector	16
3.2.1 The Central Tracking System	16
3.2.2 The dE/dx Measurement	20
3.2.3 Time-of-Flight System	21
3.2.4 Electromagnetic Calorimeter	22
3.2.5 Hadron Calorimeter	23

3.2.6	Muon Chambers	24
4	Tau Selection	25
4.1	Event Samples	25
4.1.1	OPAL Data Sample	25
4.1.2	Monte Carlo Event Sample	26
4.2	Selection of $e^+e^- \rightarrow \tau^+\tau^-$ Events	27
4.2.1	Final Tau Pair Sample	30
5	Electron Selection	31
5.1	The $\tau^- \rightarrow e^- \bar{\nu}_e \nu_\tau$ Decay	31
5.2	Electron Selection Specifications	34
5.2.1	The Dominant $\tau^- \rightarrow e^- \bar{\nu}_e \nu_\tau$ Topological Decay	34
	N_{tracks}	35
	Electromagnetic Calorimeter Geometry Requirements	35
	Energy Loss (dE/dx) Requirements	36
	Number of dE/dx hits:	36
	$N_{dE/dx}^\sigma$:	37
	Cluster Requirements	39
	E/p and $N_{E/p}^\sigma$	40
	Hadron Calorimeter Requirements	43
	Bhabha Rejection Requirements	45
5.2.2	Photon Conversions	45
5.2.3	$\tau^- \rightarrow e^- \bar{\nu}_e \nu_\tau$ Decays With No Associated Cluster	47
5.2.4	Split Tracks	49
5.3	Electron Selection Results	51
6	Background Analysis	52
6.1	$\tau^- \rightarrow h^- \geq 1\pi^0 \nu_\tau$	53
6.2	$\tau^- \rightarrow h^- \nu_\tau$	55
6.3	Other τ decay modes	56

6.4	$e^+e^- \rightarrow e^+e^-$	56
6.5	$e^+e^- \rightarrow (e^+e^-)e^+e^-$	57
7	Branching Ratio Determination	59
7.1	Branching Ratio Results	59
7.2	Systematic Errors	59
7.2.1	Photon Conversion Uncertainty	61
7.2.2	Electron Selection Efficiency	61
8	Discussion of Results	65
8.1	Branching Ratio	65
8.2	Lepton Universality	67
9	Conclusion	71
	Bibliography	72

List of Tables

2.1	Lepton and Quark masses. The Quark masses given refer to <i>constituent quark masses</i> ([5] p. 444, [7] p. 1436).	6
2.2	Standard Model particles grouped into left-handed weak isospin doublets, $T_3 = \pm\frac{1}{2}$, and right-handed singlets $T_3 = 0$. Y is the weak hypercharge and Q is the electric charge in units of the positron charge.	7
4.1	Detector and Trigger Status Requirements	26
4.2	Good track and cluster definitions.	27
4.3	Tau-pair selection requirements.	29
4.4	Non-tau background in the tau pair sample.	30
5.1	Dominant electron selection topological requirements.	35
5.2	Correction factors for $N_{dE/dx}^\sigma$	37
5.3	Parameters for $N_{E/p}^\sigma$	41
5.4	Monte Carlo Correction Factors for Electrons	43
5.5	Correction factors for N_{layers}^{HCAL}	45
5.6	Extra Requirements for photon conversions	47
5.7	Extra Requirements for split track jets	49
6.1	The backgrounds in the $\tau^- \rightarrow e^- \bar{\nu}_e \nu_\tau$ sample. The numbers given are fractions of tau decays. The first column displays the fractions taken directly from the Monte Carlo while the second column displays the corrected fractions after the data and Monte Carlo have been compared.	53

LIST OF TABLES

vii

7.1	Branching ratio data	60
7.2	Systematic Errors	60
7.3	Efficiency Systematic Errors	64

List of Figures

1.1	Lepton transitions through gauge boson interaction, where g , g' and e are the coupling constants.	2
1.2	Feynman diagrams of $\tau^- \rightarrow e^- \bar{\nu}_e \nu_\tau$ and $\tau^- \rightarrow \mu^- \bar{\nu}_\mu \nu_\tau$ decays.	3
1.3	Feynman diagrams of $\tau^- \rightarrow e^- \bar{\nu}_e \nu_\tau$ and $\mu^- \rightarrow e^- \bar{\nu}_e \nu_\mu$ decays.	3
2.1	The form of the coupling is shown for the electromagnetic, charged and neutral weak interactions.	9
2.2	Tree-level Feynman diagram where the particle labelling is shown for the matrix element \mathcal{M}	10
2.3	An example of a first order Feynman diagram with radiative emission. . .	11
3.1	(a) Schematic view of the injection scheme for LEP. (b) The main LEP ring along with the locations of the four experimental areas.	17
3.2	The Overview of the OPAL Detector.	18
3.3	Schematic view of part of one of the 24 jet chamber sectors. Anode wires depicted with "×" symbols and potential wires with "•" symbols.	20
3.4	Specific ionization measurements (dE/dx) for various particle species. . .	21
5.1	The $\tau^- \rightarrow e^- \bar{\nu}_e \nu_\tau$ decay topologies.	33
5.2	The number of tracks per jet (N_{tracks}) passing all of the other electron selection cuts is plotted both linearly and logarithmically. The points are the data, the open histogram is the Monte Carlo prediction for the $\tau^- \rightarrow e^- \bar{\nu}_e \nu_\tau$ decays, the hatched histogram is the Monte Carlo prediction for the background. The arrow indicates where the selection cut is applied.	36

5.3 The value of $N_{dE/dx}^\sigma$ is plotted both linearly and logarithmically for data (solid points) and Monte Carlo (open histogram) passing the other electron selection requirements. The hatched histogram represents the Monte Carlo prediction for the background and the arrow indicates where the selection cut was applied. 38

5.4 The number of clusters associated to a track, N_{acl} , passing all of the other electron selection cuts is plotted both linearly and logarithmically. The points are the data, the open histogram is the Monte Carlo prediction for the $\tau^- \rightarrow e^- \bar{\nu}_e \nu_\tau$ decays, and the hatched histogram is the Monte Carlo prediction for the background. 39

5.5 The number of neutral clusters passing all of the other electron selection cuts is plotted both linearly and logarithmically. The points are the data, the open histogram is the Monte Carlo prediction for the $\tau^- \rightarrow e^- \bar{\nu}_e \nu_\tau$ decays, the hatched histogram is the Monte Carlo prediction for the background and the arrow indicates where the selection cut is applied. 40

5.6 The plots on the left side show the variable E/p for $p < 5$ GeV (excluding the requirement in question), while the plots on the right side show the variable $N_{E/p}^\sigma$ both linearly and logarithmically. The points are the data, the open histogram is the Monte Carlo prediction for the $\tau^- \rightarrow e^- \bar{\nu}_e \nu_\tau$ decays, the hatched histogram is the Monte Carlo prediction for the background and the arrows indicate where the selection cut was applied. 42

5.7 N_{layers}^{HCAL} is plotted before (left side) and after (right side) corrections are applied for jets passing all of the other electron selection cuts. N_{layers}^{HCAL} is plotted both linearly and logarithmically. The points are the data, the open histogram is the Monte Carlo prediction for the $\tau^- \rightarrow e^- \bar{\nu}_e \nu_\tau$ decays, the hatched histogram is the Monte Carlo prediction for the background and the arrow indicates where the selection cut is applied. 44

- 5.8 The acoplanarity angle for events selected by the nominal electron selection, where the track has momentum $p \geq 30$ GeV and the track in the opposite hemisphere has $p \geq 0.75 E_{beam}$ is plotted linearly and logarithmically. The points are the data, the open histogram is the Monte Carlo prediction for the $\tau^- \rightarrow e^- \bar{\nu}_e \nu_\tau$ decays and the hatched histogram is the Monte Carlo prediction for the background and the arrow indicates where the selection cut was applied. 46
- 5.9 The momenta and the variable $N_{dE/dx}^\sigma$ are shown for the second track in 2 track jets for events that pass all of the other electron selection cuts. The sum of the momenta and the $N_{dE/dx}^\sigma$ are shown for the second and third tracks for 3 track jets. The last plot gives the squared invariant mass of the second and third tracks in 3 track jets. The points are the data, the open histogram is the Monte Carlo prediction for the $\tau^- \rightarrow e^- \bar{\nu}_e \nu_\tau$ decays, the hatched histogram is Monte Carlo prediction for the background, and the arrows indicate where the electron selection cut was made for that particular variable. 48
- 5.10 (a) The number of CJ hits added together for all two track jets in the tau-pair data ($N_{CJ}^{hits}(1) + N_{CJ}^{hits}(2)$), where split track candidates have $N_{CJ}^{hits}(1) + N_{CJ}^{hits}(2) < 200$. (b) The $mod(\phi, 15^\circ)$ for two track jets and $N_{CJ}^{hits}(1) + N_{CJ}^{hits}(2) < 200$. As can be seen the Monte Carlo does not model the data near the anode plane ($mod(\phi, 15^\circ) = 7.5^\circ$); the data between the arrows are the split track candidates and are kept for further analysis. For both plots the points are the data and the open histogram is the tau Monte Carlo. . . 50
- 6.1 The left plot shows the jet mass for electron candidates with $N_{neutral} = 1$ and $p \geq 5$ GeV; the points are hadron candidates, the open histogram is the Monte Carlo prediction for hadrons and the hatched histogram is the electron contribution. The right plot shows a similar plot but with the $N_{dE/dx}^\sigma$ requirement reversed so that hadrons are selected. 54

6.2	The normalised E/p variable, $N_{E/p}^\sigma$, for electron candidates with $N_{neutral} = 0$ and $p \geq 5$ GeV but with the $N_{dE/dx}^\sigma$ requirement reversed so that hadrons are selected. The unhatched part of the histogram is the $\tau^- \rightarrow h^- \nu_\tau$ contribution, while the hatched part is from hadrons accompanied by π^0 's. . .	55
6.3	(a) The shower energy, $\Sigma E_{clus}/E_{beam}$ after the $\tau^- \rightarrow e^- \bar{\nu}_e \nu_\tau$ selection. (b) Expanded view of the shower energy. For both plots the histogram is the combined $e^+e^- \rightarrow \tau^+\tau^-$ and $e^+e^- \rightarrow e^+e^-$ Monte Carlo, the points are the data and the hatched histogram is the $e^+e^- \rightarrow e^+e^-$ background. . .	57
6.4	(a) The visible energy, $(\Sigma E_{clus} + \Sigma p_{track})/E_{CM}$ after the $\tau^- \rightarrow e^- \bar{\nu}_e \nu_\tau$ selection. (b) Expanded view of the visible energy. For both plots the histogram is the combined $e^+e^- \rightarrow \tau^+\tau^-$ and $e^+e^- \rightarrow (e^+e^-)e^+e^-$ Monte Carlo, the points are the data and the hatched histogram is the $e^+e^- \rightarrow (e^+e^-)e^+e^-$ Monte Carlo background.	58
7.1	The $\tau^- \rightarrow e^- \bar{\nu}_e \nu_\tau$ branching ratio versus different cut values. The points are the branching ratio values, including the relative systematic errors between the different cut values and the best cut value. The solid line is the electron branching ratio.	62
7.2	The $\tau^- \rightarrow e^- \bar{\nu}_e \nu_\tau$ branching ratio versus different cut values. The points are the branching ratio values, including the relative systematic errors between the different cut values and the best cut value. The solid line is the electron branching ratio. Note that the error bars are smaller than the data points in all four plots.	63
8.1	The electronic branching ratio of this work is compared to other recent measurements. The errors are the quadratic sum of the statistical and systematic errors. The band represents the error specified for the Particle Data Group $\tau^- \rightarrow e^- \bar{\nu}_e \nu_\tau$ branching ratio value. The Particle Data Group number is a weighted average of measurements up to 1994. Those measurements below the dashed line are included in the Particle Data Group number.	66

8.2	Electron-muon universality results of this work compared to other measurements. The pion and W decay results are taken directly from the references. The dotted line gives the value assuming electron-muon universality. . . .	68
8.3	Tau-muon universality results of this work compared to other measurements. The results that use $B(\tau^- \rightarrow e^- \bar{\nu}_e \nu_\tau)$ are calculated using equation (2.14). The W decay results are taken directly from the references. The dotted line gives the value assuming tau-muon universality.	69
8.4	The OPAL lifetime measurement is plotted against the tau electronic branching ratio. The band displays the standard model relation between these quantities for a tau mass of $m_\tau = 1777.1_{-0.5}^{+0.4}$ MeV.	70

Acknowledgements

I would like to thank Randy Sobie for his help in understanding this analysis, his critical reading, useful comments and to agreeing to be my supervisor for this thesis. I would like to thank Paul Poffenberger and Richard Keeler for their critical reading and constructive comments about this thesis. I would like to thank Myron Rosvick for help with scanning the Jet Chamber picture and for discussions that helped me understand the OPAL detector better. I would also like to thank Manuella Vincter for writing the clustering algorithm that was used in this analysis.

Chapter 1

Introduction

The Standard Model describes the interaction of particles under the influence of the strong, weak and electromagnetic forces. The strong interaction is described by the theory of Quantum Chromodynamics, while the weak and electromagnetic interactions are described by the unified electroweak theory. This thesis will test aspects of the electroweak theory of the Standard Model through the study of the weak decay of the tau to an electron and two neutrinos.

Leptons are fundamental particles of nature having no observed substructure. Charged leptons can interact both through the weak and electromagnetic interactions, while the neutral leptons or neutrinos only interact via the weak interaction. Currently there are three known charged leptons: e^- , μ^- and τ^- ; and three known neutrinos: ν_e , ν_μ , and ν_τ . The first observed elementary particle, the electron, was discovered in 1897 by Thomson. The muon was detected in cosmic rays in the 1930's [1], and the last discovered charged lepton, the tau, was observed in high energy e^-e^+ collisions by M. Perl *et. al.* in 1975 [2]. The electron neutrino was postulated by Pauli around 1931 [3] and was observed by Reines and Cowen in 1953 [4] by studying inverse beta decay. The existence of the muon neutrino has also been confirmed while the tau neutrino has not been experimentally verified.

The interaction of leptons with the electroweak force is shown symbolically in Fig. 1.1. A lepton l^- may emit or absorb a photon (Fig. a). An example of this interaction is the photoelectric effect, where an atomic electron absorbs a photon. Similarly a lepton l^- may

emit or absorb a Z^0 (Fig. b). In addition, a lepton l^- may emit or absorb a W^- (Fig. c). In this case the outgoing lepton ν_l carries no charge.

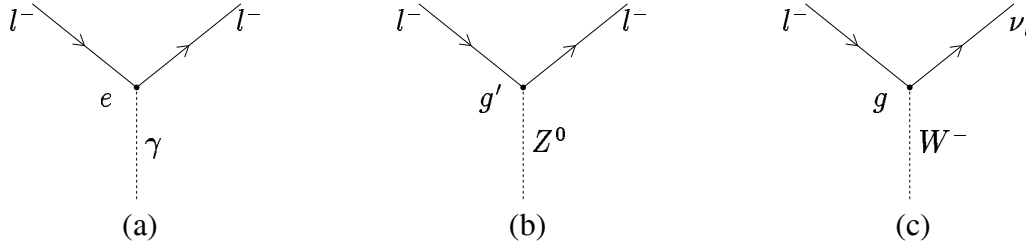


Figure 1.1: Lepton transitions through gauge boson interaction, where g , g' and e are the coupling constants.

The Standard Model predicts the form of the interaction between the leptons, but not the strength of the coupling between them. The coupling constant must be measured experimentally. The coupling constants for the three lepton transitions are indicated in Fig. 1.1, where g and g' are the weak coupling constants for the W^\pm and Z^0 interactions respectively, and e is the electromagnetic coupling constant. The Standard Model assumes that the couplings are not dependent on the lepton family, *i.e.* $g_e = g_\mu = g_\tau$. This is known as *lepton universality*. Any deviation from the Standard Model assumption could indicate new physics.

Lepton universality can be tested by several methods. Electron-muon universality can be tested by studying the decays of the pion, W boson, and the tau lepton, while tau-muon universality can be tested by studying the decays of the W boson and the tau lepton. This analysis will examine lepton universality by studying decays of the tau lepton. If the tau is a heavy version of the electron or the muon leptons, then the coupling of the leptons to the W boson should be the same. Electron-muon universality can be examined by comparing the decay widths of the $\tau^- \rightarrow e^- \bar{\nu}_e \nu_\tau$ decay and the $\tau^- \rightarrow \mu^- \bar{\nu}_\mu \nu_\tau$ decay. Note that the decay notations used throughout this thesis also imply the charged conjugate decays, *i.e.* $\tau^+ \rightarrow e^+ \nu_e \bar{\nu}_\tau$ and $\tau^+ \rightarrow \mu^+ \nu_\mu \bar{\nu}_\tau$. The Feynman diagrams of these decays are given in Fig. 1.2. Similarly, tau-muon universality can be examined by comparing the decay widths

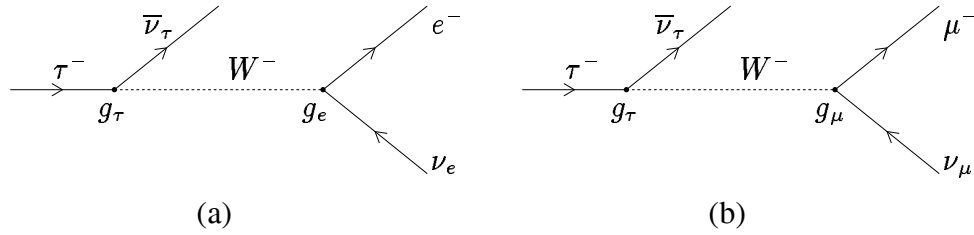


Figure 1.2: Feynman diagrams of $\tau^- \rightarrow e^- \bar{\nu}_e \nu_\tau$ and $\tau^- \rightarrow \mu^- \bar{\nu}_\mu \nu_\tau$ decays.

of the $\tau^- \rightarrow e^- \bar{\nu}_e \nu_\tau$ decay and the $\mu^- \rightarrow e^- \bar{\nu}_e \nu_\mu$ decay. The Feynman diagrams of these decays are given in Fig. 1.3.

The probability of the τ^- decaying to $e^- \bar{\nu}_e \nu_\tau$ is related to the decay width $\Gamma(\tau^- \rightarrow e^- \bar{\nu}_e \nu_\tau)$. The decay width depends on kinematic factors, and the form and strength of the interaction. The width of the $\tau^- \rightarrow \mu^- \bar{\nu}_\mu \nu_\tau$ decay, $\Gamma(\tau^- \rightarrow \mu^- \bar{\nu}_\mu \nu_\tau)$, has the same form as $\Gamma(\tau^- \rightarrow e^- \bar{\nu}_e \nu_\tau)$, except that m_e and g_e must be replaced by m_μ and g_μ . Consequently the ratio of the widths $\Gamma(\tau^- \rightarrow e^- \bar{\nu}_e \nu_\tau)/\Gamma(\tau^- \rightarrow \mu^- \bar{\nu}_\mu \nu_\tau)$ gives a measurement of g_e/g_μ . Similarly, tau-muon universality can be tested by comparing the decay widths of the $\tau^- \rightarrow e^- \bar{\nu}_e \nu_\tau$ and $\mu^- \rightarrow e^- \bar{\nu}_e \nu_\mu$ decays, giving a measurement of g_τ/g_μ .

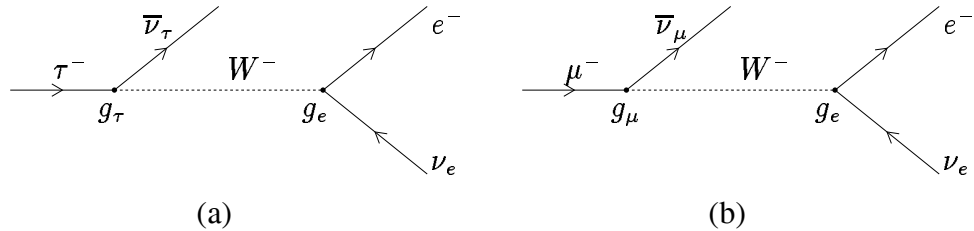


Figure 1.3: Feynman diagrams of $\tau^- \rightarrow e^- \bar{\nu}_e \nu_\tau$ and $\mu^- \rightarrow e^- \bar{\nu}_e \nu_\mu$ decays.

The tau can decay into many different final states. The branching ratio $B(\tau \rightarrow x)$ is defined to be the fraction of times a particle decays into a particular final state. For example, the tau decays to the $e^- \bar{\nu}_e \nu_\tau$ final state approximately 18% of the time. This thesis will present a new measurement of the $\tau^- \rightarrow e^- \bar{\nu}_e \nu_\tau$ branching ratio, and use that branching

ratio, along with measurements of $\tau^- \rightarrow \mu^- \bar{\nu}_\mu \nu_\tau$ and $\mu^- \rightarrow e^- \bar{\nu}_e \nu_\mu$ from OPAL¹ and other experiments, to test the hypothesis of lepton universality.

At LEP², tau leptons are produced through the reaction $e^+e^- \rightarrow Z^0 \rightarrow \tau^+\tau^-$. LEP is an e^+e^- colliding beam synchrotron which is presently capable of providing beam energies up to 55 GeV. It has been in operation since August 1989 at a centre-of-mass energy of about 91 GeV, which is approximately the mass of the Z^0 resonance. Four multipurpose detectors, DELPHI³, ALEPH⁴, L3⁵, and OPAL, are installed at beam interaction regions. The data used in this analysis were accumulated by the OPAL detector between 1991-1994.

An outline of the rest of the thesis will now be presented. In chapter 2 a further description of the Standard Model will be given. The decay width and the formulation of the charged current universality relations between g_e, g_μ and g_τ will be described. Chapter 3 describes the OPAL detector used to take the data that were analysed in this analysis. Chapter 4 describes the OPAL data, the simulated (Monte Carlo) data and describes the tau pre-selection. Chapter 5 describes the $\tau^- \rightarrow e^- \bar{\nu}_e \nu_\tau$ selection requirements. Chapter 6 discusses the background in the $\tau^- \rightarrow e^- \bar{\nu}_e \nu_\tau$ sample. In chapter 7, the $\tau^- \rightarrow e^- \bar{\nu}_e \nu_\tau$ branching ratio is calculated, and the error analysis of the branching ratio is discussed. Chapter 8 will compare and contrast the results of this analysis with other recent results and discuss lepton universality and chapter 9 has some concluding remarks about the analysis of the $\tau^- \rightarrow e^- \bar{\nu}_e \nu_\tau$ decay and lepton universality.

¹Omni Purpose Apparatus for LEP

²Large Electron Positron collider

³Detector with Lepton Photon and Hadron Identification

⁴Apparatus for LEP Physics

⁵LEP 3 experiment

Chapter 2

Theory

In the first section of this chapter the Standard Model will be reviewed. The $\tau^- \rightarrow e^- \bar{\nu}_e \nu_\tau$ decay width is discussed in the second section. The third section shows how the $\tau^- \rightarrow e^- \bar{\nu}_e \nu_\tau$ decay width can be used with other measurements to test lepton universality. The last section describes how the $\tau^- \rightarrow e^- \bar{\nu}_e \nu_\tau$ branching ratio can be determined.

2.1 Standard Model

The Standard Model [5, 6] describes the interaction of elementary particles. This interaction is mediated by the four fundamental forces of nature: electromagnetic, weak, strong and gravitational forces. The electromagnetic interaction is characterised by the emission or exchange of a photon which couples to the electrical charge of the interacting particle. The weak force occurs by exchanging one of three intermediate vector bosons. The strong force is mediated by gluons which are responsible for binding quarks together into hadrons. The gravitational force is the weakest force, having no measurable effects on a subatomic scale.

The elementary particles can be categorised as leptons or quarks, whose masses are shown in Table 2.1. The charged leptons, such as the electron, can interact via both the weak and electromagnetic interactions, while the neutral leptons or neutrinos only interact via the weak interaction. Hadrons, such as the pion are composed of quarks and can interact through the strong interaction, in addition to the weak and electromagnetic interactions.

Leptons	Mass (GeV/ c^2)	Quarks	Mass (GeV/ c^2)
ν_e	$< 5.1 \times 10^{-9}$	u	0.33
e	5.11×10^{-4}	d	0.34
ν_μ	$< 2.7 \times 10^{-4}$	c	1.55
μ	0.106	s	0.54
ν_τ	$< .03$	t	176
τ	1.78	b	4.80

Table 2.1: Lepton and Quark masses. The Quark masses given refer to *constituent quark masses* ([5] p. 444, [7] p. 1436).

The form of the forces between the elementary particles is determined by the principle of local gauge invariance, that is, the particles have some properties which can be interchanged without changing the force. For example, quarks have colour (red, green or blue) and the colours can be interchanged without changing the strength of the strong interaction. The rules for interchanging the properties are specified by a gauge group.

The Standard Model is based on the gauge group $SU_c(3) \times SU_L(2) \times U_Y(1)$. The $SU_c(3)$ colour group generates quantum chromodynamics (QCD), while the $SU_L(2) \times U_Y(1)$ group is responsible for the electroweak interactions. The $SU_L(2)$ group is responsible for the weak interactions, and together with the $U_Y(1)$ group can be shown to generate QED, the theory of electromagnetic interactions. The quantum number associated with the $U_Y(1)$ group is called the weak hypercharge Y .

The subscript L on $SU_L(2)$ is due to the experimental observation that the charged currents in weak interactions couple only to fermions with left-handed helicity. Helicity is defined as $\mathcal{H} = 2\vec{J} \cdot \hat{p}$, where \vec{J} is the particle's spin and \hat{p} is a unit vector in the direction of the momentum. The left-handed helicity charged lepton and its associated neutrino form a weak isospin doublet under $SU_L(2)$ (see Table 2.2). Similarly, pairs of quarks with left-handed helicity form weak isospin doublets. The fermion charge, Q , is related to Y

Fermions			T	T_3	Y	Q
$\begin{pmatrix} \nu_e \\ e \end{pmatrix}_L$	$\begin{pmatrix} \nu_\mu \\ \mu \end{pmatrix}_L$	$\begin{pmatrix} \nu_\tau \\ \tau \end{pmatrix}_L$	1/2	1/2	-1	-1
$\begin{pmatrix} u \\ d \end{pmatrix}_L$	$\begin{pmatrix} c \\ s \end{pmatrix}_L$	$\begin{pmatrix} t \\ b \end{pmatrix}_L$	1/2	-1/2	-1	0
e_R	μ_R	τ_R	0	1/2	1/3	2/3
u_R	c_R	t_R	0	-1/2	1/3	-1/3
d_R	s_R	b_R	0	0	-2	-1
			0	0	4/3	2/3
			0	0	-2/3	-1/3

Table 2.2: Standard Model particles grouped into left-handed weak isospin doublets, $T_3 = \pm \frac{1}{2}$, and right-handed singlets $T_3 = 0$. Y is the weak hypercharge and Q is the electric charge in units of the positron charge.

and T_3 , the third component of the weak isospin, by

$$Q = T_3 + \frac{Y}{2}.$$

The right-handed fermions are put into the theory as weak isospin singlets. There are no right-handed helicity components for massless neutrinos.

Glashow, Salam, and Weinberg [8] unified the weak interactions with electromagnetism by postulating the electroweak force. The electroweak force has to include the three gauge fields associated with the $SU_L(2)$ group ($W_\mu^1, W_\mu^2, W_\mu^3$) and another associated with the $U_Y(1)$ group, B_μ . But the associated gauge bosons are massless, in contradiction to the experimental observations by both the UA1 and UA2 collaborations [9] of the very large masses of the physical W and Z bosons. The problem is solved by having an underlying vacuum, or the lowest energy state, that contains a field, called the Higgs, with a non-zero expectation value. The Higgs particle couples to mass but the coupling constant and Higgs mass itself are not specified by the theory. This process, referred to as the *Higgs mechanism*, gives mass to the gauge bosons.

The Higgs mechanism generates a non-diagonal mass matrix for the two neutral gauge

bosons. Diagonalising the mass matrix gives the physical fields,

$$\begin{aligned} Z_\mu &= \cos \theta_W W_\mu^3 + \sin \theta_W B_\mu \\ A_\mu &= \cos \theta_W B_\mu - \sin \theta_W W_\mu^3, \end{aligned} \quad (2.1)$$

where A_μ is the photon field and Z_μ is the Z^0 boson. The other two gauge bosons, the W^+ and W^- bosons, are given as linear combinations of the first two fields of the $SU_L(2)$ group,

$$W^\pm = \sqrt{\frac{1}{2}}(W_\mu^1 \mp iW_\mu^2). \quad (2.2)$$

The mixing angle θ_W is related to the intrinsic $SU_L(2)$ and $U_Y(1)$ couplings, g and g' , respectively by

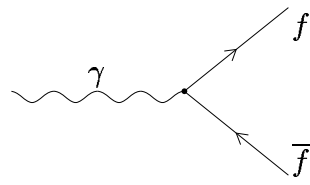
$$g \sin \theta_W = g' \cos \theta_W = e = \sqrt{4\pi\alpha}, \quad (2.3)$$

where α is the fine structure constant and e is the positron's electric charge. The mixing angle θ_W is called the Weinberg angle and has been determined experimentally to be $\sin^2 \theta_W = 0.2311 \pm 0.0009$ [7].

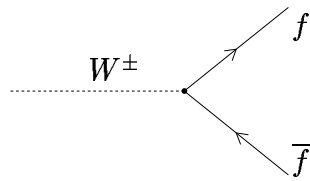
The Standard Model specifies the coupling constants between the fermions (f) and gauge bosons (γ, W^\pm, Z^0) in terms of $\sin \theta_W$. The Feynman diagrams for electromagnetic, charged and neutral weak couplings are given in Fig. 2.1, where γ^μ are the Dirac matrices. The term $(1 - \gamma^5)$ in the charged weak interaction represents the fact that this interaction is purely left-handed. The neutral weak interaction contains vector (v_f) and axial-vector (a_f) factors which indicate that there are both left-handed and right-handed components in this interaction.

2.2 The Decay Width

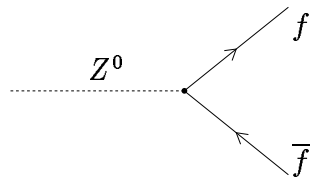
The rate of decay of the tau is given by its total width Γ_τ . The mean lifetime of the tau is inversely proportional to the total width. The tau can decay to many different final states, so the total width is the algebraic sum of the individual, or partial decay widths. The branching ratio of the tau to a particular final state is the ratio of the partial decay width to the total decay width. For example, $B(\tau^- \rightarrow e^- \bar{\nu}_e \nu_\tau) = \Gamma(\tau^- \rightarrow e^- \bar{\nu}_e \nu_\tau) / \Gamma_\tau$.



$$Q\bar{u}(f)\gamma^\mu u(f)A_\mu$$



$$\frac{g}{\sqrt{2}}\bar{u}(f)\gamma^\mu(1-\gamma^5)u(f)W_\mu$$



$$\frac{g}{2\cos\theta_W}\bar{u}(f)\gamma^\mu(v_f - a_f\gamma^5)u(f)Z_\mu$$

Figure 2.1: The form of the coupling is shown for the electromagnetic, charged and neutral weak interactions.

The differential width for the decay of any particle can be written as [6]

$$d\Gamma = \frac{1}{2m} |\mathcal{M}|^2 dLips, \quad (2.4)$$

where \mathcal{M} is the transition amplitude, or matrix element, and $dLips$ is the Lorentz invariant phase space factor,

$$dLips = \frac{d^3 p_2}{(2\pi)^3 2E_2} \frac{d^3 p_3}{(2\pi)^3 2E_3} \frac{d^3 p_4}{(2\pi)^3 2E_4} (2\pi)^4 \delta^{(4)}(p_1 - p_2 - p_3 - p_4),$$

where the p_i are the four-vectors of the particles (see Fig. 2.2).

The matrix element, \mathcal{M} , for the $\tau^- \rightarrow l^- \bar{\nu}_l \nu_\tau$ decay can be derived from the Feynman diagram given in Fig. 2.2. It can be written as

$$\mathcal{M} = \frac{g_l g_\tau}{8m_W^2} [\bar{u}(\bar{\nu}_\tau) \gamma^\mu (1 - \gamma^5) u(\tau^-)] [\bar{u}(l^-) \gamma_\mu (1 - \gamma^5) u(\nu_l)], \quad (2.5)$$

where u and \bar{u} are Dirac spinors.

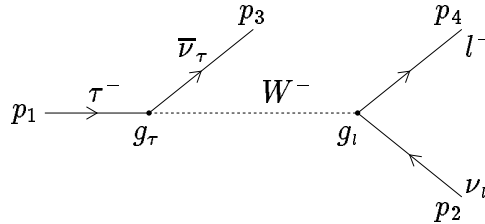


Figure 2.2: Tree-level Feynman diagram where the particle labelling is shown for the matrix element \mathcal{M} .

Assuming a point interaction, the spin averaged square of the matrix element is

$$|\mathcal{M}|^2 = 2 \left(\frac{g_l g_\tau}{m_W^2} \right)^2 (p_1 \cdot p_2)(p_3 \cdot p_4), \quad (2.6)$$

where the p_i are the four-vectors of the particles (see Fig. 2.2).

The integration of the differential in equation (2.4) gives [10, 11],

$$\Gamma(\tau^- \rightarrow l^- \bar{\nu}_l \nu_\tau) = \frac{g_l^2 g_\tau^2}{(8m_W^2)^2} \frac{m_\tau^5}{96\pi^3} f\left(\frac{m_l^2}{m_\tau^2}\right) \quad (2.7)$$

where $f(x) = (1 - 8x + 8x^3 - x^4 - 12x^2 \ln x)$ and the masses of the neutrinos are taken as zero. For the $\tau^- \rightarrow e^- \bar{\nu}_e \nu_\tau$ decay, $f\left(\frac{m_e^2}{m_\tau^2}\right) = 1.0000$ and for the $\tau^- \rightarrow \mu^- \bar{\nu}_\mu \nu_\tau$ decay, $f\left(\frac{m_\mu^2}{m_\tau^2}\right) = 0.9726$.

2.2.1 Higher Order Corrections

The tree-level Feynman diagram is the dominant contribution to the decay width. However there are higher order Feynman diagrams that also contribute to the width of the $\tau^- \rightarrow l^- \bar{\nu}_l \nu_\tau$ decay. The largest type of higher order correction is from electromagnetic radiative emission (see Fig. 2.3).

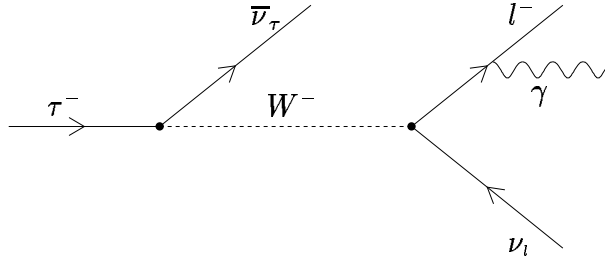


Figure 2.3: An example of a first order Feynman diagram with radiative emission.

Radiative corrections can be represented by Feynman diagrams, as in Fig. 2.3, with extra photons added to the tree level diagram as either a real bremsstrahlung photon or a virtual photon loop. The fractional change in the width due to all radiative corrections is calculated to be [12]

$$\frac{\delta\Gamma}{\Gamma} = \frac{\alpha(m_\tau)}{2\pi} \left(\frac{25}{4} - \pi^2 \right), \quad (2.8)$$

where $\alpha(m_\tau)$ is the fine structure constant evaluated at the mass of the tau. Thus for $\alpha(m_\tau) = 1/133.3$, the radiative correction suppresses the rate of the tau decay by approximately 0.4%. Note that the probability of a $\tau^- \rightarrow e^- \bar{\nu}_e \nu_\tau$ decay accompanied by photons is estimated using simulated data (Monte Carlo).

The decay width calculation can also be corrected for the finite W boson mass. The corrections to the W propagator have been studied in considerable detail in references [13, 14]. The tree-level corrections for the $\tau^- \rightarrow l^- \bar{\nu}_l \nu_\tau$ decay width has the form

$$1 + \frac{3}{5} \frac{m_\tau^2}{m_W^2} - 2 \frac{m_l^2}{m_W^2}. \quad (2.9)$$

Using $m_W = 80.22$ GeV [7] and the lepton masses from Table 2.1, the W boson mass correction increases the decay rate by approximately 0.03% for both the $\tau^- \rightarrow e^- \bar{\nu}_e \nu_\tau$ and $\tau^- \rightarrow \mu^- \bar{\nu}_\mu \nu_\tau$ decays.

2.2.2 The Total Width

The total width of the $\tau^- \rightarrow l^- \bar{\nu}_l \nu_\tau$ decay, including electromagnetic radiative corrections and tree level corrections to the W propagator, is [14, 15]

$$\Gamma(\tau^- \rightarrow l^- \bar{\nu}_l \nu_\tau) = \frac{g_l^2 g_\tau^2}{(8m_W^2)^2} \frac{m_\tau^5}{96\pi^3} f\left(\frac{m_l^2}{m_\tau^2}\right) \left(1 + \frac{3m_\tau^2}{5m_W^2} - \frac{2m_l^2}{m_W^2}\right) \left[1 + \frac{\alpha(m_\tau)}{2\pi} \left(\frac{25}{4} - \pi^2\right)\right]. \quad (2.10)$$

Note that $\Gamma(\tau^- \rightarrow l^- \bar{\nu}_l \nu_\tau)$ includes both the lepton and photons in the final state. Marciano and Sirlin [16] have shown that most of the electroweak corrections can be absorbed in the couplings, and the remainder absorbed in the fine structure constant $\alpha(m_\tau)$. Corrections up to order $(\alpha/2\pi)m_l^2/m_\tau^2$ have been included.

2.3 Lepton Universality

Lepton universality traditionally has been used to describe the fact that, neglecting mass effects, the electron, muon and tau leptons all exhibit identical properties. In the standard model, universality implies that the three generations of leptons all have the same $SU_L(2) \times U_Y(1)$ transformation properties and quantum numbers. As a result, their intrinsic gauge couplings given in equation (2.3) must be identical:

$$\begin{aligned} g_e &= g_\mu = g_\tau = g, \\ g'_e &= g'_\mu = g'_\tau = g'. \end{aligned} \quad (2.11)$$

One can test the universality of the g coupling by comparing the lepton decay modes of the tau and muon. A comparison of the $\tau^- \rightarrow e^- \bar{\nu}_e \nu_\tau$ and $\mu^- \rightarrow e^- \bar{\nu}_e \nu_\mu$ decays gives a measure of g_τ/g_μ while a comparison of the $\tau^- \rightarrow e^- \bar{\nu}_e \nu_\tau$ and $\tau^- \rightarrow \mu^- \bar{\nu}_\mu \nu_\tau$ decays gives a measure of g_e/g_μ . Any deviation from unity in either of these quantities would imply *new physics*.

The ratio of the widths for the $\tau^- \rightarrow e^- \bar{\nu}_e \nu_\tau$ and $\tau^- \rightarrow \mu^- \bar{\nu}_\mu \nu_\tau$ decays, which equals the ratio of the respective branching ratios, including electromagnetic radiative corrections

and tree level corrections to the W propagator, is related to g_e and g_μ through

$$\frac{\Gamma(\tau^- \rightarrow e^- \bar{\nu}_e \nu_\tau)}{\Gamma(\tau^- \rightarrow \mu^- \bar{\nu}_\mu \nu_\tau)} = \frac{B(\tau^- \rightarrow e^- \bar{\nu}_e \nu_\tau)}{B(\tau^- \rightarrow \mu^- \bar{\nu}_\mu \nu_\tau)} = \frac{g_e^2}{g_\mu^2} \left[\frac{f\left(\frac{m_e^2}{m_\tau^2}\right)}{f\left(\frac{m_\mu^2}{m_\tau^2}\right)} \right]. \quad (2.12)$$

The ratio of the widths for the $\tau^- \rightarrow e^- \bar{\nu}_e \nu_\tau$ and $\mu^- \rightarrow e^- \bar{\nu}_e \nu_\mu$ decays can be written as

$$\frac{\Gamma(\tau^- \rightarrow e^- \bar{\nu}_e \nu_\tau)}{\Gamma(\mu^- \rightarrow e^- \bar{\nu}_e \nu_\mu)} = K \frac{g_\tau^2 m_\tau^5}{g_\mu^2 m_\mu^5}, \quad (2.13)$$

where

$$K = \frac{f\left(\frac{m_e^2}{m_\tau^2}\right) \left(1 + \frac{3m_\tau^2}{5m_W^2} - 2\frac{m_e^2}{m_W^2}\right) \left[1 + \frac{\alpha(m_\tau)}{2\pi} \left(\frac{25}{4} - \pi^2\right)\right]}{f\left(\frac{m_\mu^2}{m_\tau^2}\right) \left(1 + \frac{3m_\mu^2}{5m_W^2} - 2\frac{m_\mu^2}{m_W^2}\right) \left[1 + \frac{\alpha(m_\mu)}{2\pi} \left(\frac{25}{4} - \pi^2\right)\right]} = 1.00039.$$

The ratio of the tau and muon couplings can therefore be written in terms of the electronic branching ratios of the tau and muon and their lifetimes, T_μ and T_τ respectively, to obtain

$$\frac{g_\tau^2}{g_\mu^2} = \frac{1}{K} \frac{T_\mu}{T_\tau} B(\tau^- \rightarrow e^- \bar{\nu}_e \nu_\tau) \left[\frac{m_\mu}{m_\tau}\right]^5, \quad (2.14)$$

where we have used $\Gamma(\tau^- \rightarrow e^- \bar{\nu}_e \nu_\tau) = B(\tau^- \rightarrow e^- \bar{\nu}_e \nu_\tau)/T_\tau$ and $\Gamma(\mu^- \rightarrow e^- \bar{\nu}_e \nu_\mu) = B(\mu^- \rightarrow e^- \bar{\nu}_e \nu_\mu)/T_\mu$, and where it is assumed that $B(\mu^- \rightarrow e^- \bar{\nu}_e \nu_\mu) = 100\%$ [7].

In this thesis we measure the $\tau^- \rightarrow e^- \bar{\nu}_e \nu_\tau$ branching ratio, $B(\tau^- \rightarrow e^- \bar{\nu}_e \nu_\tau)$. Together with other measurements of the tau lifetime and mass, muon lifetime and mass and $B(\tau^- \rightarrow \mu^- \bar{\nu}_\mu \nu_\tau)$ one can test lepton universality. The next section will describe how the $\tau^- \rightarrow e^- \bar{\nu}_e \nu_\tau$ branching ratio is determined in this analysis.

2.4 The $\tau^- \rightarrow e^- \bar{\nu}_e \nu_\tau$ Branching Ratio Formulation

The $B(\tau^- \rightarrow e^- \bar{\nu}_e \nu_\tau)$ branching ratio is defined to be the number of $\tau^- \rightarrow e^- \bar{\nu}_e \nu_\tau$ decays, N_e , including radiative decays, divided by the total number of tau decays N_τ in the data:

$$B(\tau^- \rightarrow e^- \bar{\nu}_e \nu_\tau) = \frac{N_e}{N_\tau}. \quad (2.15)$$

The sample of tau decays, N_τ^{sel} , was selected by applying the tau-pair selection algorithm, as will be described in Chapter 4, on the full data sample. This selection allows a

small fraction of non-tau decays, f_{bkgd}^τ , into the selected tau decay sample, N_τ^{sel} . Therefore, the true number of tau decays in the sample can be written as

$$N_\tau = (1 - f_{bkgd}^\tau) N_\tau^{sel}. \quad (2.16)$$

The f_{bkgd}^τ and N_τ^{sel} will be determined in Chapter 4.

Next, the selection of the $\tau^- \rightarrow e^- \bar{\nu}_e \nu_\tau$ candidates from the tau-pair sample is done. This will remove some of the $\tau^- \rightarrow e^- \bar{\nu}_e \nu_\tau$ events from the sample, and will also allow some non-electron events into the final event sample. The actual number N_e of $\tau^- \rightarrow e^- \bar{\nu}_e \nu_\tau$ events in the selected tau decay sample will therefore be given by the number of selected $\tau^- \rightarrow e^- \bar{\nu}_e \nu_\tau$ candidates, N_e^{sel} , corrected for the background contamination, f_{bkgd}^e , and the selection efficiency, ϵ_e . Therefore

$$N_e = (1 - f_{bkgd}^e) \frac{N_e^{sel}}{\epsilon_e}. \quad (2.17)$$

The selection efficiency, ϵ_e , is determined by observing the fraction of true $\tau^- \rightarrow e^- \bar{\nu}_e \nu_\tau$ events that are removed when the $\tau^- \rightarrow e^- \bar{\nu}_e \nu_\tau$ selection are applied to the tau-pair simulated data (Monte Carlo). The efficiency is corrected for the observed differences between the data and Monte Carlo after some geometry requirements are applied.

Finally, the tau-pair selection requirements may preferentially remove certain event topologies, altering the apparent branching ratios in the selected tau sample. The measured branching ratio must be corrected for the selection bias, F_{bias}^e , in order to determine the true branching ratio. This quantity has been determined by applying the tau-pair selection requirements to the tau-pair Monte Carlo and observing the ratio of the fraction of $\tau^- \rightarrow e^- \bar{\nu}_e \nu_\tau$ events before the tau-pair selection to the same fraction after selection. This ratio is $F_{bias}^e = 1.0036 \pm 0.0022$ [34].

Therefore the $\tau^- \rightarrow e^- \bar{\nu}_e \nu_\tau$ branching ratio is determined by combining equations (2.15),(2.16) and (2.17), and correcting for the tau-pair bias, resulting in

$$B(\tau^- \rightarrow e^- \bar{\nu}_e \nu_\tau) = \frac{N_e^{sel}}{N_\tau^{sel}} \frac{1 - f_{bkgd}^e}{1 - f_{bkgd}^\tau} \frac{1}{\epsilon_e} \frac{1}{F_{bias}^e}. \quad (2.18)$$

The $\tau^- \rightarrow e^- \bar{\nu}_e \nu_\tau$ branching ratio and its uncertainty will be calculated in Chapter 7.

Chapter 3

The OPAL Experiment

This chapter will describe the experimental facility used to collect the data that were used for this analysis. The first section will describe the Large Electron Positron (LEP) [17] collider facility at CERN just outside Geneva, Switzerland. The second section describes the OPAL detector and its components which were used to collect the data for this analysis.

3.1 The LEP Collider

The LEP collider facility consists of several different particle accelerators that are used to create high energy electrons and positrons and bring them into collision. The injector chain produces and accelerates electrons and positrons to 20 GeV, while the main ring accelerates the particles to approximately 45 GeV, providing the centre-of-mass energy of 90 GeV required for Z^0 physics.

Fig. 3.1(a) shows a schematic diagram of the LEP injector chain. Positrons are produced by directing electrons from a 200 MeV linac onto a converter target. The electrons and positrons are then accelerated in a 600 MeV linac and collected in the Electron-Positron Accumulator (EPA). After accumulation in the EPA, the electrons and positrons are injected into the Proton Synchrotron (PS) where they are accelerated to 3.5 GeV and then transferred to the Super Proton Synchrotron (SPS) which then accelerates the particles to 20 GeV. The final acceleration to 45 GeV is done in the LEP ring.

The LEP ring is 26.66 km in circumference and is buried between 100 m and 150 m underground (see Fig.3.1(b)). The collider was designed to provide a peak luminosity of $1.6 \times 10^{31} \text{cm}^{-2}\text{s}^{-1}$ at an average beam current of 3 mA. LEP has been operated in four and eight bunch mode. In four bunch mode there are four equally spaced bunches each of electrons and positrons which are made to collide at eight intersection points, four of which are instrumented with large detectors.

3.2 The OPAL Detector

OPAL is one of four large detectors whose purpose is to detect all types of interactions occurring in e^+e^- collisions at a centre of mass energy of about 90 GeV. A full description of the detector can be found in reference [18] and a schematic of the OPAL detector is shown in Fig. 3.2.

The coordinate system used by OPAL is illustrated in Fig. 3.2; the x -axis is horizontal and points toward the centre of LEP, the y axis is vertical, and the z -axis is in the e^- beam direction. The origin of the coordinate system is at the nominal interaction point at the centre of the detector. The polar angle, θ , is measured from the z -axis about the x -axis, and the azimuthal angle, ϕ , is measured from the x -axis about the z -axis.

3.2.1 The Central Tracking System

The central tracking system consists of a silicon microvertex detector and three drift chamber devices: the vertex chamber, the jet chamber and the z -chamber. The central tracking system operates at a pressure of 4 bar and is therefore contained inside a pressure vessel whose cylindrical structure provides mechanical support to the solenoidal magnet mounted around it. The solenoidal magnet maintains a uniform field strength of 0.435 Tesla. Only two of these detectors are used in this analysis: the vertex chamber and the jet chamber. They are described below.

The Central Vertex chamber (CV) is a high resolution cylindrical drift chamber which extends radially from 80 mm to 235 mm from the interaction point. The detector is

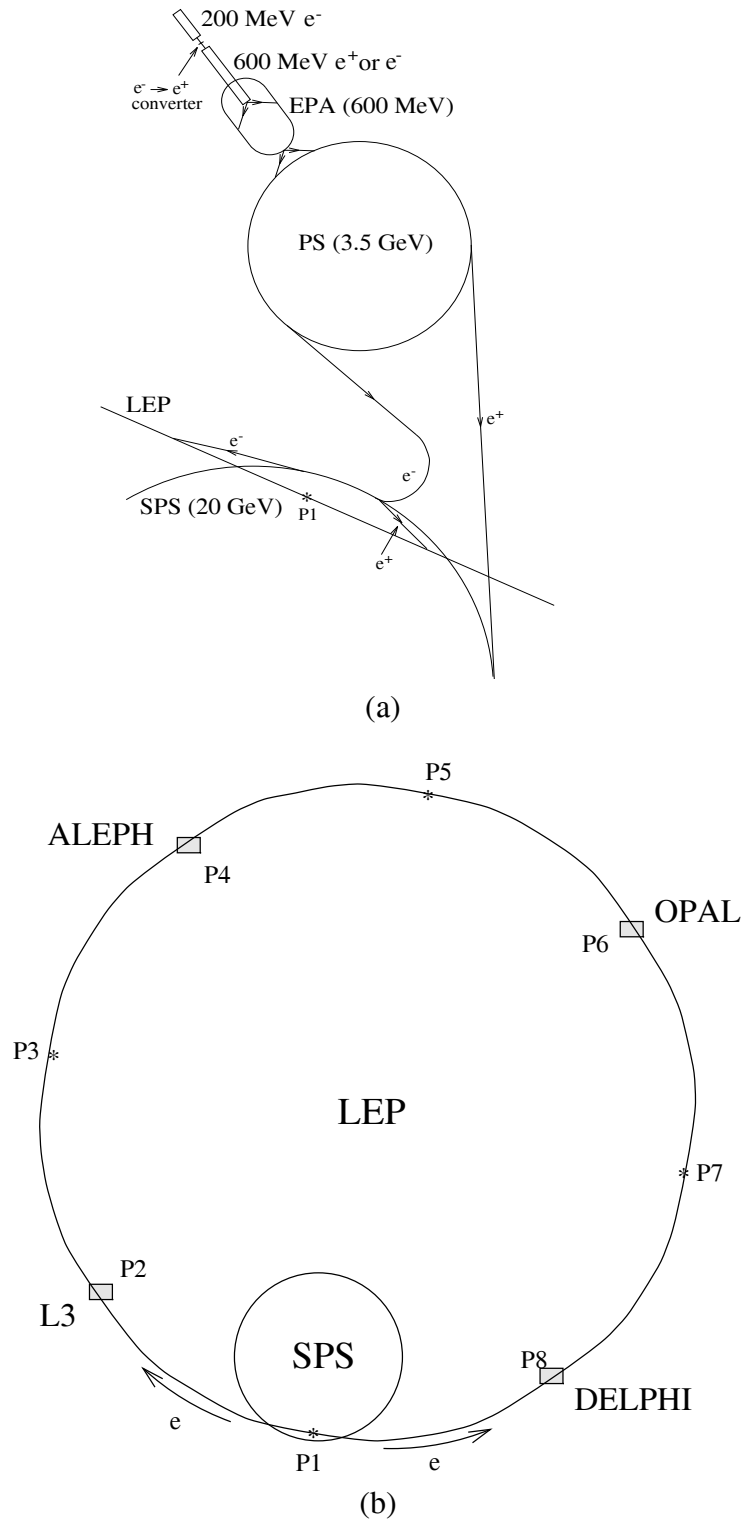


Figure 3.1: (a) Schematic view of the injection scheme for LEP. (b) The main LEP ring along with the locations of the four experimental areas.

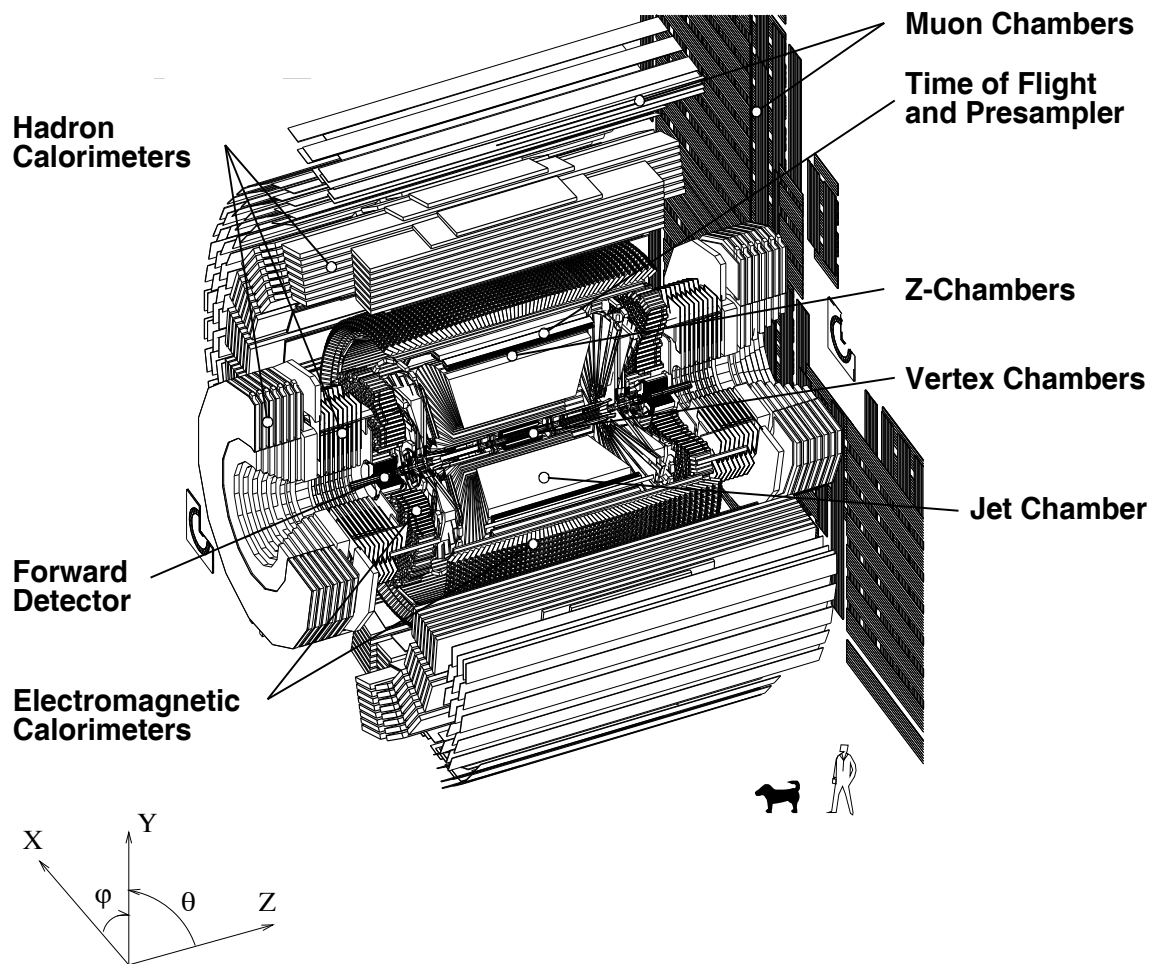


Figure 3.2: The Overview of the OPAL Detector.

composed of an inner layer of thirty-six axial wire cells, each composed of twelve anode sense wires, and an outer layer of thirty six stereo cells inclined at 4° , each with six anode wires. The drift time to the axially placed sense wires can be measured precisely enough so that the position of a track in the $r - \phi$ plane is calculated with a resolution of $55 \mu\text{m}$. The time difference between signals at either end of the sense wires gives a fast but relatively coarse z coordinate measurement which is used by the OPAL track triggering and in pattern recognition. A measurement of this quantity to a precision of 0.1 ns allows the z -coordinate to be determined to ~ 4 cm. The vertex chamber has *stereo* layers, which are tilted at a small angle with respect to the axial layers. The combination of stereo layer and axially placed sense wire information provides an accurate z measurement for charged particles close to the interaction region, with a combined resolution of $700 \mu\text{m}$.

The Central Jet chamber (CJ) is a large cylindrical drift chamber with a length of approximately 4 m with conical end planes and is divided into 24 identical sectors in ϕ each containing a sense wire plane with 159 anode wires and two cathode wire planes that form the boundaries between adjacent sectors. The anode wires are located between radii of 255 mm and 1835 mm, equally spaced by 10 mm and alternating with potential wires. To resolve left-right ambiguities, the anode wires are staggered by $\pm 100 \mu\text{m}$ alternately to the left and right side of the plane defined by the potential wires. A schematic drawing of a section of a jet chamber sector is shown in Fig. 3.3. Similar to the vertex chamber, a measurement of the drift time determines the coordinates of wire hits of a track in the $r - \phi$ plane with a resolution of $135 \mu\text{m}$ at the mean drift distance of 7 cm, and the ratio of the charges between the signals at either end of the wires gives a measure of the z -position with a resolution of 6 cm. The ionization energy loss of the charged particles, dE/dx , is measured by integrating the charge received at each end of a wire allowing identification of particles by determining the velocity and momentum simultaneously. The dE/dx will be discussed in further detail in the next section.

The momentum of the particle is obtained by measuring the curvature of the particle track in the magnetic field. The momentum resolution for the jet chamber is given by

$$\frac{\sigma_{p_T}}{p_T} = \sqrt{(0.0004 + (0.0015 \times p_T)^2)},$$

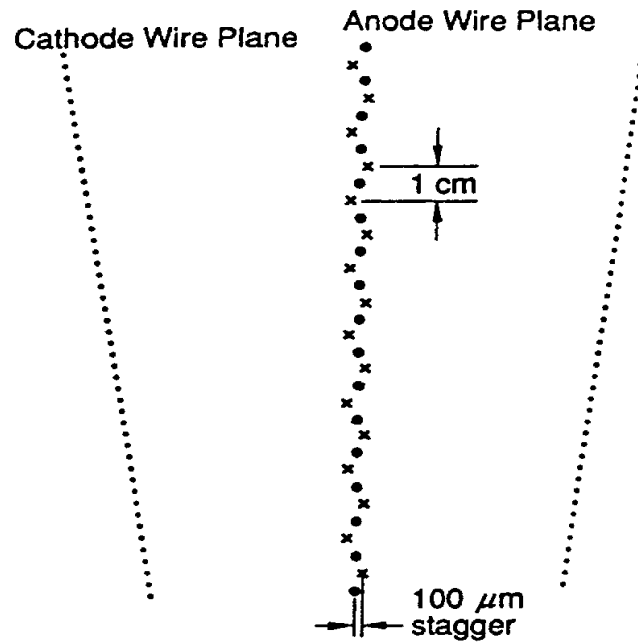


Figure 3.3: Schematic view of part of one of the 24 jet chamber sectors. Anode wires depicted with "×" symbols and potential wires with "•" symbols.

where p_T in GeV/c is the momentum component transverse to the beam direction [19].

3.2.2 The dE/dx Measurement

The energy loss of a particle is measured as it travels through the gas in the Central Jet chamber (CJ). The CV, CJ and CZ detectors are all contained in a pressure vessel maintained at a pressure of 4 bar, optimised to provide the best dE/dx resolution for particle separation.

As stated in the previous section, the charge deposited on each wire is proportional to the energy loss of the particle as it travels through the OPAL jet chamber. The independent energy loss measurements are distributed according to a Landau distribution from which the mean energy loss for each particle can be measured. The resolution of the dE/dx

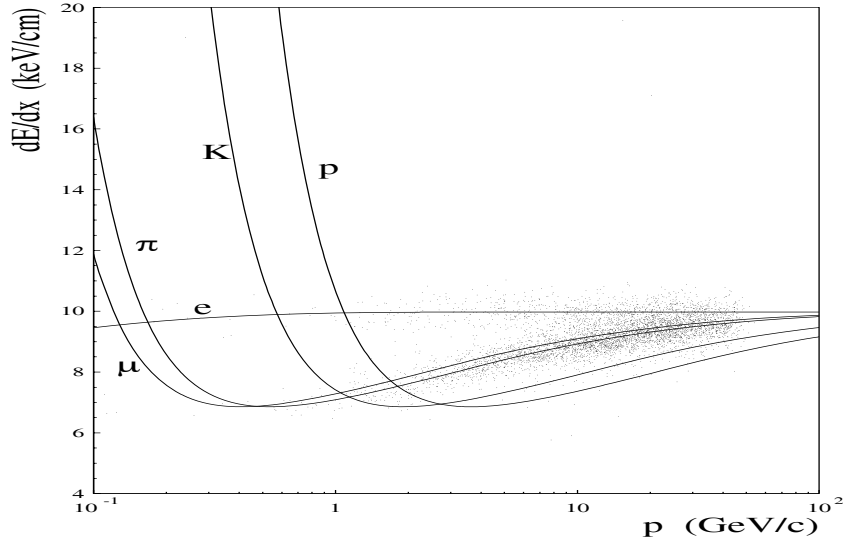


Figure 3.4: Specific ionization measurements (dE/dx) for various particle species.

measurement for the OPAL jet chamber has been determined to be [21]

$$\frac{\sigma(dE/dx)}{(dE/dx)} = \sigma_{159} \left(\frac{159}{N_{sample}} \right)^{0.43}, \quad (3.1)$$

where N_{sample} is the number of wire hits in the CJ detector that are used to measure dE/dx and σ_{159} is the resolution obtained when all the 159 dE/dx samples are used in the energy loss measurements. Typically the dE/dx resolution is from 3-4%. Note that most tracks do not have 159 hits due to the application of hit quality criteria. Fig. 3.4 shows the dependence of dE/dx on the momentum for various particle species.

3.2.3 Time-of-Flight System

Surrounding the tracking detectors and magnet is the time-of-flight (TOF) system. The TOF system covers the barrel region (TB), $|\cos \theta| < 0.82$, of the OPAL detector. It is comprised of 160 scintillation counters, at an average radius of 2.36 m. It generates trigger signals and allows charged particle identification in the range 0.6 – 2.5 GeV. The TOF provides a timing resolution of 460 ps for muons and a z -resolution of 5.5 cm. The z -

position is measured by comparing the time difference between the signals at the ends of the scintillators. In this analysis the TOF detector is used for cosmic ray rejection.

3.2.4 Electromagnetic Calorimeter

The electromagnetic calorimeter at OPAL (ECAL) is outside both the pressure vessel of the tracking system and the coil of the magnet. It consists of a pre-shower counter (pre-sampler) and a lead glass calorimeter. The electromagnetic calorimeter is designed to contain and measure the energy and position of electrons, positrons, and photons. Muons leave very little energy, while hadrons may leave a substantial fraction of their energy in the electromagnetic calorimeter.

It is convenient to measure the thickness of the ECAL material in units of the radiation length X_0 , the mean distance over which a high energy electron loses all but $1/e$ of its energy by bremsstrahlung. It is therefore an appropriate scale of length for describing high-energy electromagnetic cascades [7]. The material in front of the calorimeter (*i.e.* the solenoid, central detector and pressure vessel *etc.*) is approximately two radiation lengths thick and causes a slight degradation of the energy and spatial resolutions because of electromagnetic showering before the lead glass.

The electromagnetic pre-sampler is located immediately in front of the electromagnetic calorimeter. It consists of two concentric cylinders of limited streamer tubes with wires parallel to the beam axis and cathode strips oriented at $\pm 45^\circ$ with respect to the wires. The pre-sampler samples the energy of a particle after it passes through the magnetic coil, enabling one to make a correction if the shower has started in the coil.

The barrel region (EB) of the electromagnetic calorimeter covers $|\cos \theta| < 0.82$ and the endcap region (EE) covers $|\cos \theta|$ from 0.81 to 0.95. For this analysis, only those events fully contained in the barrel region are used. The barrel electromagnetic calorimeter consists of two half-ring sections that form a cylindrical array of 9440 lead-glass blocks with 59 blocks in the z -direction and 160 blocks in the ϕ direction. Each block is $24.6X_0$ thick (where $X_0 = 1.5$ cm for the lead-glass) with an area of approximately $10 \text{ cm} \times 10 \text{ cm}$. Located 2455 mm from the beam, this corresponds to an angular coverage of approximately

40 mr \times 40 mr. The blocks are oriented so that they point back toward the interaction point with a slight offset to minimise the possibility that a particle will pass through a crack between the blocks. Note that where the half-ring sections come together, the calorimeter measurements may not be accurate. To solve this problem, this region of the electromagnetic calorimeter is excluded from the analysis. The energy resolution of the electromagnetic calorimeter including the material between the calorimeter and the interaction region is $\sigma_E/E = (1.8\% + 23\%/\sqrt{E})$, where E is measured in GeV [22]. Lead-glass was chosen for the electromagnetic calorimeter because of its excellent intrinsic energy resolution ($\sigma_E/E \sim 5\%/\sqrt{E}$), linearity, spatial resolution (~ 1 cm), granularity, electron-hadron discrimination, hermiticity and gain stability. Cerenkov light produced by relativistic charged particles in the blocks is detected by phototubes at the base of each block.

3.2.5 Hadron Calorimeter

Outside the electromagnetic calorimeter is the iron return yoke of the magnet, which is instrumented using streamer tubes with pads and strips to form a hadron calorimeter (HCAL). The hadron calorimeter consists of three parts: the barrel (HB) covering $|\cos \theta| < 0.81$, the endcap (HE) covering $0.815 < |\cos \theta| < 0.91$, and the pole tip (HT) covering $0.91 < |\cos \theta| < 0.99$. In this analysis, only the barrel hadron calorimeter is used in the electron selection. The iron of the return yoke is divided into eight 10 cm thick slabs which provide over four interaction lengths of absorber material (an interaction length is the mean free path between hadronic interactions). These slabs are interleaved with nine 25 mm thick streamer tubes, usually called HCAL layers, which act as the active material of the calorimeter. The HCAL strips (HS) give signals which are used to count the number of particles reaching each layer. Since there is a high probability of hadronic interactions being initiated in the 2.2 interaction lengths of material before the hadron calorimeter, the overall hadronic energy is measured by combining the signals of the electromagnetic calorimeter and the hadron calorimeter. The energy resolution of the hadron calorimeter is $120\%/\sqrt{E}$, where E is in GeV.

3.2.6 Muon Chambers

Outside the hadron calorimeter are four layers of drift chambers, which identify muons by range. Most electrons, hadrons and photons are stopped by the calorimeters. The chambers measure the position and direction of all charged particles leaving the hadron calorimeter. Ninety-three percent of the solid angle is covered by at least one layer of the muon chamber, with some gaps in the acceptance due to the beam pipe, the supporting legs and the cables. Each layer is constructed of 110 large-area drift chambers, 1.2 m wide and 90 mm deep. The barrel region (MB) covers $|\cos \theta| < 0.68$ for at least four layers; the endcap region (ME) covers $0.67 < |\cos \theta| < 0.98$.

Chapter 4

Tau Selection

This chapter will present the selection of the tau events used in this analysis. The first section describes the OPAL data as well as the Monte Carlo simulated data samples that were used to estimate efficiencies and backgrounds in the data sample. The second section discusses the selection of tau pair decays of the Z^0 from the full data set.

4.1 Event Samples

4.1.1 OPAL Data Sample

The data used in this analysis were taken during the 1991-1994 running periods of LEP. The OPAL detector information is read out when the trigger identifies some activity that coincides with the beam crossing [18]. The raw data are processed in real time so that background from beam-gas interactions and cosmic rays are reduced. The data are then passed through a reconstruction program (ROPE) [23] which converts the raw information (*eg.* drift times) to physical quantities (*eg.* tracks).

It is important that only reliably measured quantities be used for the selection criteria. Therefore the subdetectors used to make the measurements are required to be in good running order during the data taking period. There are four status levels defined for each subdetector: 0 indicates that the subdetector status is unknown, 1 indicates that it is off, 2 means that the detector is partly on, and 3 indicates the detector is fully on. Table 4.1

	CV	CJ	TB	PB	EB	EE	HS	MB
detector	3	3	3	2	3	3	3	3
trigger	-	2	-	-	2	3	-	-

Table 4.1: Detector and Trigger Status Requirements

shows the levels required for each detector used in this analysis; if there is no status level indicated then no requirement was placed on that particular trigger.

4.1.2 Monte Carlo Event Sample

Monte Carlo simulated data were used to estimate the selection efficiency and backgrounds in this analysis. The primary Monte Carlo event sample of four-vector quantities for the reaction $e^+e^- \rightarrow \tau^+\tau^-$ was generated using the KORALZ [24] simulation program. KORALZ simulates tau pair production and decays at the Z^0 centre-of-mass energy, including higher order corrections.

Decays of the taus produced by KORALZ are simulated using the TAULO1.5 [25] program. The branching ratios used in KORALZ were the world averages at the time that the Monte Carlo data sample was created, however the selection method does not rely on their particular values.

A total of 300,000 tau-pair events were generated. The four-vectors of the particles were processed by the OPAL detector simulation program, GOPAL [26], which uses the program GEANT [27] to track the particles through the volume of the OPAL detector. GOPAL produces output in an identical format (with the addition of the initial four-vectors) as the data that are extracted from the OPAL detector. The Monte Carlo sample is then passed through the same reconstruction procedure as the real data.

	Requirements	Variable Description
Track definition	$N_{CJ}^{hits} \geq 20$ hits	N_{CJ}^{hits} : number of hits in the jet chamber.
	$p_T \geq 0.1$ GeV	p_T : momentum transverse to the beam direction.
	$ d_0 \leq 2$ cm	$ d_0 $: point of closest approach of the track to the interaction point in the $x - y$ plane.
	$ z_0 \leq 75$ cm	$ z_0 $: point of closest approach of the track to the interaction point in the z -direction.
	$R_{min} \leq 75$ cm	R_{min} : radius of the first jet chamber hit.
Cluster definition	$N_{blocks} \geq 1$	N_{blocks} : number of calorimeter blocks in the cluster.
	$E_{clusters} \geq 0.1$ GeV	$E_{clusters}$: total energy in the cluster.

Table 4.2: Good track and cluster definitions.

4.2 Selection of $e^+e^- \rightarrow \tau^+\tau^-$ Events

This section describes the procedure used to reduce the full event sample to a relatively pure sample of events containing tau-pairs produced in Z^0 decays. This tau selection algorithm was developed by the OPAL tau working group. Complete details of the tau pair selection criteria can be found in references [28, 29].

The final state of the $e^+e^- \rightarrow Z^0 \rightarrow \tau^+\tau^-$ reaction is characterised by two back-to-back taus. The taus are relativistic and their decay products are collimated, so it is convenient to treat each tau as a jet which is defined as a cone of half-angle 35° [30]. Each tau decays to 1–5 charged tracks and 1–5 clusters, where the definitions of a track and cluster are given in Table 4.2.

The selection criteria for tau-pair events is given in Table 4.3. To begin the tau-pair selection, a tau-pair candidate must contain exactly two jets, each with at least one charged track and with a total track and cluster energy that exceeds 1% of the beam energy. The average value of $|\cos \theta|$ for the two charged jets must satisfy $|\cos \theta|_{ave} < 0.68$ to avoid the

interface region between the barrel and endcap of the lead-glass calorimeter.

The tau-pair selection must eliminate the other Z^0 decays, such as quark-antiquark ($q\bar{q}$), e^+e^- , or $\mu^+\mu^-$ final states; and also from other reactions, such as the two photon reaction $e^+e^- \rightarrow (e^+e^-)X$, where X is any lepton pair. These background contaminations of the tau-pair sample will be discussed below.

Multihadronic events, $e^+e^- \rightarrow q\bar{q}$ are reduced by limiting the number of tracks and clusters in the event, as previously discussed. Multihadronic background is easier to discriminate at LEP than at lower-energy experiments because the particle multiplicity in $e^+e^- \rightarrow q\bar{q}$ events increase with E_{CM} , while for tau-pair events it remains constant.

Electron-pair final states, $e^+e^- \rightarrow e^+e^-$, can be identified by the presence of two high-momentum, back-to-back charged particles with the full centre-of mass energy (E_{CM}) deposited in the lead-glass electromagnetic calorimeter. This background can be reduced by requiring tau-pair candidates to satisfy either $\sum E_{cluster} \leq 0.8E_{CM}$ or $\sum E_{cluster} + 0.3 \sum E_{track} \leq E_{CM}$, where $E_{cluster}$ is the total energy in the lead-glass calorimeter and E_{track} is the total energy of the charged tracks in the event.

Muon-pair final states, $e^+e^- \rightarrow \mu^+\mu^-$, can be identified by the presence of two high-momentum, back-to-back charged particles but with very little energy deposited in the lead-glass electromagnetic calorimeter. Events are rejected if they pass the muon-pair selection as given in Table 4.3.

Two-photon events $e^+e^- \rightarrow (e^+e^-)e^+e^-$, $e^+e^- \rightarrow (e^+e^-)\mu^+\mu^-$ and $e^+e^- \rightarrow (e^+e^-)\tau^+\tau^-$ contain a final state electron and positron that escape undetected at low angles. These backgrounds are small because they lack the enhancement to the cross-section from the Z^0 resonance and because the visible energy (the sum of the charged track and lead-glass cluster energies) of the two-photon system is in general much smaller than that from a tau-pair event.

Cosmic rays are the final background contamination of the tau-pair sample. The Cosmic ray background is negligible with simple requirements on the time-of-flight detector and on the location of the primary event vertex. A complete description of all the tau-pair requirements is shown in Table 4.3

	Requirements	Variable Description
Good event	$N_{jet} = 2$	N_{jet} : No. of jets satisfying the E_{jet} requirement.
	$ \cos\theta _{ave} < 0.68$	$ \cos\theta _{ave}$: average value of $ \cos\theta $ for the 2 jets.
	$E_{jet} \geq 0.01E_{beam}$	E_{jet} : total track and cluster energy in the jet. E_{beam} : the beam energy.
Multihadron Rejection	$1 \leq N_{track} \leq 6$	N_{track} : No. of tracks in a jet.
	$N_{clusters} \leq 10$	$N_{clusters}$: No. of clusters in a jet.
e^+e^- Rejection	$\sum E_{cluster} \leq 0.8E_{CM}$ or $\sum E_{cluster} + 0.3 \sum E_{track} \leq E_{CM}$	
$\mu^+\mu^-$ Rejection	$\sum_{jets}(E_{cluster}^{total} + E_{track}) \leq 0.6E_{CM}$ and a jet is a muon.	
	A jet is a muon if one of the following is true:	
	$N_{layers}^{MUON} \geq 2$	N_{layers}^{MUON} : total No. of layers in the barrel or endcap muon detector with signals associated to the track.
	$E_{cluster} < 2 \text{ GeV}$	$E_{cluster}$: Energy of the ECAL cluster ass. to the track.
	$N_{layers}^{HCAL} \geq 4$ $N_{outer\ 3\ layers}^{HCAL} \geq 1$ and $N_{hits/layers}^{HCAL} < 2$	N_{layers}^{HCAL} : number of hadron calorimeter layers with signals associated to the track. $N_{outer\ 3\ layers}^{HCAL}$: No. of signals in 3 outer HCAL layers. $N_{hits/layers}^{HCAL}$: total number of calorimeter signals assigned to the jet divided by N_{layers}^{HCAL} .
Two-photon Rejection	$\theta_{acol} \leq 15^\circ$	θ_{acol} : the angle between the 2 jet directions and the jet directions are given by the momentum sums of the tracks and clusters.
	$E_{vis} \geq 0.03E_{CM}$	$E_{vis} = \sum_{cone} Max(E_{cluster}, E_{track})$ $E_{CM} = 2E_{beam}$
	If $E_{vis} \leq 0.20E_{CM}$ then $p_T(cluster) > 2.0 \text{ GeV}$ or $p_T(track) > 2.0 \text{ GeV}$	
Cosmic ray Rejection	$ d_0 _{min} \leq 5 \text{ mm}$	$ d_0 _{min}$: minimum d_0 for all tracks in the event.
	$ z_0 _{min} \leq 20 \text{ cm}$	$ z_0 _{min}$: minimum z_0 for all tracks in the event.
	$ z_0 _{ave} \leq 20 \text{ cm}$	$ z_0 _{ave}$: average z_0 for all tracks in the event.
	$ t_{meas} - t_{exp} \leq 10 \text{ ns}$	t_{meas} and t_{exp} : measured and expected times of flight assuming the event is created at the origin.
	If $ \phi_i - \phi_j \geq 165^\circ$ then reject the event if $ t_i - t_j \geq 10 \text{ ns}$.	

Table 4.3: Tau-pair selection requirements.

4.2.1 Final Tau Pair Sample

A total of 83474 tau-pairs were selected from the 1991-1994 data and 162879 tau-pairs were identified by the tau-pair selection from the Monte Carlo sample giving a tau-pair selection efficiency of $54.3 \pm 0.1\%$, which corresponds to an efficiency of 93% within the geometrical acceptance of the detector. The background contamination estimated from the Monte Carlo event samples is found to be 0.0183 ± 0.0030 [31], with the individual contributions described above, summarised in Table 4.4.

Background	Contamination
$e^+e^- \rightarrow e^+e^-$	0.0024 ± 0.0007
$e^+e^- \rightarrow \mu^+\mu^-$	0.0100 ± 0.0028
$e^+e^- \rightarrow q\bar{q}$	0.0042 ± 0.0008
$e^+e^- \rightarrow (e^+e^-)e^+e^-$	0.0009 ± 0.0002
$e^+e^- \rightarrow (e^+e^-)\mu^+\mu^-$	0.0008 ± 0.0002
Total	0.0183 ± 0.0030

Table 4.4: Non-tau background in the tau pair sample.

Chapter 5

Electron Selection

This chapter will describe the electron selection algorithm used in this analysis. The first section discusses the various topologies of a $\tau^- \rightarrow e^- \bar{\nu}_e \nu_\tau$ decay and the methods used to find these $\tau^- \rightarrow e^- \bar{\nu}_e \nu_\tau$ decays. The second section explicitly describes the technical details of the $\tau^- \rightarrow e^- \bar{\nu}_e \nu_\tau$ selection requirements used. The last section summarises the results after the $\tau^- \rightarrow e^- \bar{\nu}_e \nu_\tau$ selection requirements have been applied to the tau-pair data.

5.1 The $\tau^- \rightarrow e^- \bar{\nu}_e \nu_\tau$ Decay

In a perfect detector the $\tau^- \rightarrow e^- \bar{\nu}_e \nu_\tau$ decay would appear as a single charged track that points to an energy deposition in the ECAL. Any additional photons would appear as distinct energy depositions in the ECAL. Most of the $\tau^- \rightarrow e^- \bar{\nu}_e \nu_\tau$ decays appear with this topology in the OPAL detector. However, the OPAL detector is not perfect; it contains material that causes photons to convert to $e^- e^+$ pairs; the magnetic field bends the low momentum electrons away from the ECAL; the coil of the magnet can prevent low momentum electrons from reaching the ECAL; and there are problems reconstructing the charged tracks when a particle passes close to the anode plane of the central drift chamber.

In Fig. 5.1 we show the topologies that are identified by the electron selection. We assume that each jet corresponds to a tau decay (see Section 4.2). Each topology represents the activity of the detector within a jet. Each consists of a *primary* track which is the highest

momentum track in the jet. Additional tracks in the jet are labelled *track #2* and *track #3*, and are ordered in descending momentum. If the position of a track at the front face of the ECAL is close to the centroid of an ECAL cluster then the cluster is assumed to have been created by the charged track and is considered to be *associated* to the primary track. Other clusters that are not-associated to the primary track are called *neutral* clusters.

Approximately 95% of the $\tau^- \rightarrow e^- \bar{\nu}_e \nu_\tau$ fall in the first or *dominant* topology shown in Fig. 5.1(a). Only one charged track is found in the jet and it is associated to an ECAL cluster. There may or may not be a neutral ECAL cluster in the jet.

About 1.5% of the sample fall in the second (Fig. 5.1(b)) and third (Fig. 5.1(c)) topologies in which a photon in the jet has converted to an $e^+ e^-$ pair. In the first of these topologies one of the tracks from the photon conversion is undetected. The fourth topology (Fig. 5.1(d)), corresponding to about 3% of the sample, are jets where the primary track is either too low in momentum to reach the ECAL (bends back toward the vertex) or not energetic enough to penetrate the magnetic coil located in front of the ECAL. The final topology (Fig. 5.1(e)) occurs when a track crosses an anode plane of the jet chamber (see Fig. 3.3) causing the track reconstruction program to form two tracks instead of one track. This latter topology is quite rare, comprising only $\sim 0.1\%$ of the final sample.

The selection of $\tau^- \rightarrow e^- \bar{\nu}_e \nu_\tau$ candidates through the dominant topology will be discussed first. The primary track is required to have a dE/dx measurement that is compatible with that expected from an electron. As shown in Fig. 3.4, muons and hadrons can be easily separated from electrons at low momentum. The ratio of E/p , the energy of the associated ECAL cluster divided by the primary track momentum, is then used to remove muons and hadrons. The number of neutral clusters is required to be 0 or 1 to reduce the background from tau decays that include π^0 's. It is required that the electron candidate penetrate no further than 2 of the 9 layers of the HCAL. Finally, the background from $e^+ e^- \rightarrow e^+ e^-$ events is reduced by requiring that the angle between the primary track in this jet with the primary track in the opposite hemisphere is greater than 0.10 degrees.

The two photon conversion topologies follow a similar selection procedure. The primary track must pass the same requirements as the dominant topology. The remaining tracks

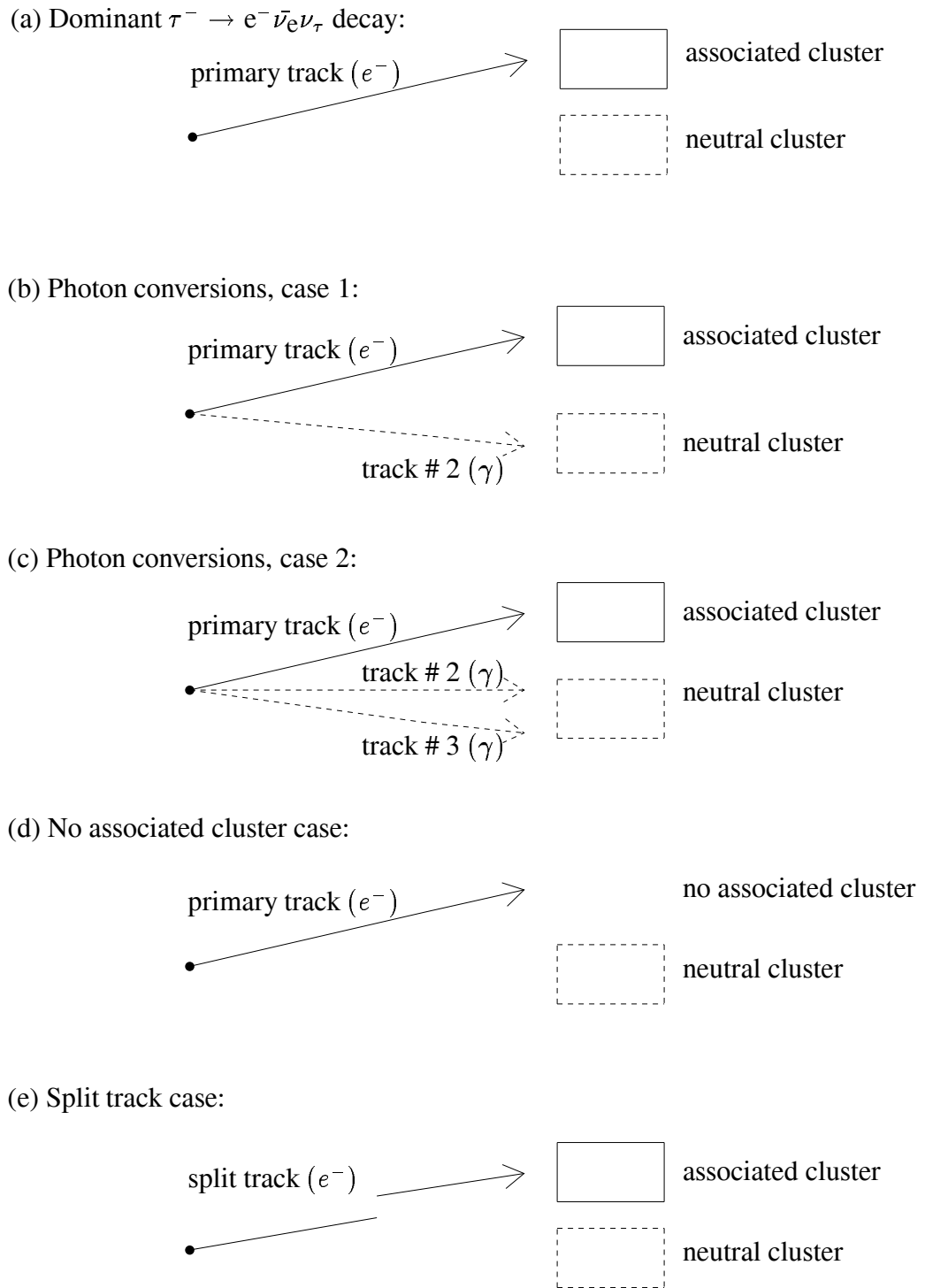


Figure 5.1: The $\tau^- \rightarrow e^- \bar{\nu}_e \nu_\tau$ decay topologies.

must pass a simple photon conversion identification algorithm. For jets containing 1 extra track, that track must pass dE/dx and momentum requirements. For jets with 2 extra tracks, both tracks must pass dE/dx and momentum requirements, as well as a mass requirement to ensure that both tracks originated from a photon.

The fourth $\tau^- \rightarrow e^- \bar{\nu}_e \nu_\tau$ decay topology studied in this analysis results from tracks that have no associated ECAL cluster. In these cases, the jet is considered to be an electron candidate if the primary track passes the above requirements for the dominant topology, with the E/p requirement removed as there is no associated cluster.

The fifth $\tau^- \rightarrow e^- \bar{\nu}_e \nu_\tau$ decay topology studied in this analysis is the *split track* case which is caused by the track crossing the anode plane of the central drift chamber. After being identified as a split track candidate, the particle must then pass the electron selection requirements for the dominant topology. The $\tau^- \rightarrow e^- \bar{\nu}_e \nu_\tau$ selection for the above topologies will now be discussed in the following section.

5.2 Electron Selection Specifications

The technical aspects of the $\tau^- \rightarrow e^- \bar{\nu}_e \nu_\tau$ selection algorithm will now be discussed. We will describe the $\tau^- \rightarrow e^- \bar{\nu}_e \nu_\tau$ decay topologies in the same order as presented in section 5.1. In section 5.3 the overall efficiency and the number of $\tau^- \rightarrow e^- \bar{\nu}_e \nu_\tau$ candidates found will be discussed.

5.2.1 The Dominant $\tau^- \rightarrow e^- \bar{\nu}_e \nu_\tau$ Topological Decay

The dominant $\tau^- \rightarrow e^- \bar{\nu}_e \nu_\tau$ topological decay requirements are given in Table 5.1. The variables listed in the Table will now be described in greater detail so that it becomes evident why the particular selection requirements were made.

Requirements	Variable Description
$N_{tracks} \leq 3$	N_{tracks} : No. of tracks in the jet.
$89.75^\circ < \phi < 90.25^\circ$ $0.213 < \cos \theta < 0.216$ $269.75^\circ < \phi < 270.25^\circ$ $0.596 < \cos \theta < 0.598$	θ & ϕ : ECAL entrance angles.
dE/dx (i) $N_{dE/dx}^{hits} \geq 40$ (ii) $N_{dE/dx}^\sigma \geq -3$	$N_{dE/dx}^{hits}$: No. of CJ hits used to calculate dE/dx . $N_{dE/dx}^\sigma$: Normalised value of dE/dx .
$N_{neutral} \leq 1$	$N_{neutral}$: No. of EB clusters in the jet with no associated track.
$N_{layers}^{HCAL} \leq 2$	N_{layers}^{HCAL} : No. of HCAL layers containing a signal
$E/p \geq 0.3$ $p < 5 \text{ GeV}$	p : Momentum of the primary track. E/p : Ratio of the associated cluster energy E to the track momentum p .
$N_{E/p}^\sigma \geq -3.5$ $p \geq 5 \text{ GeV}$	$N_{E/p}^\sigma$: the normalised value of E/p .
$\theta_{acoplanarity} \geq 0.1^\circ$ $p \geq 30$ and $x_{opp} \geq 0.75$	$\theta_{acoplanarity}$: Acoplanarity angle between the primary tracks in the two jets. x_{opp} : Momentum of the primary track of the opposite jet divided by the beam energy.

Table 5.1: Dominant electron selection topological requirements.

N_{tracks}

In Fig. 5.2, we plot the number of tracks in each jet, N_{tracks} , that pass the electron selection excluding the N_{tracks} requirement. In this analysis it is required that $1 \leq N_{tracks} \leq 3$.

Electromagnetic Calorimeter Geometry Requirements

If the extrapolated position of any of the tracks fall in the regions where the half-ring sections of the ECAL come together, the jet is rejected. These regions are listed in Table 5.1.

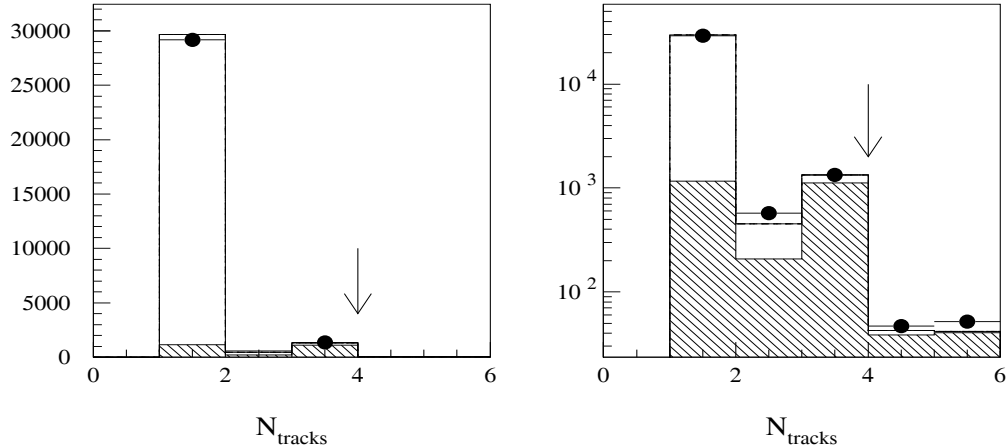


Figure 5.2: The number of tracks per jet (N_{tracks}) passing all of the other electron selection cuts is plotted both linearly and logarithmically. The points are the data, the open histogram is the Monte Carlo prediction for the $\tau^- \rightarrow e^- \bar{\nu}_e \nu_\tau$ decays, the hatched histogram is the Monte Carlo prediction for the background. The arrow indicates where the selection cut is applied.

Energy Loss (dE/dx) Requirements

The energy loss measurement, dE/dx , is used to distinguish between electrons, muons and pions at low momentum. We first apply requirements to ensure that dE/dx is well measured, then a normalised value of dE/dx is created. These are described below.

Number of dE/dx hits: A track in the central Jet Chamber can have up to 159 hits. The energy loss is considered well measured in OPAL if there are at least 40 wires with good individual measurements of the energy loss. In this analysis it was required that all tracks in the jet satisfy $N_{dE/dx}^{hits} \geq 40$.

Data Set	$(dE/dx)_{corr}$	S-factor
Data		
1991	0.	1.0
1992	0.	1.0
1993	-0.05	1.03
1994	0.03	1.10
MC 93		
electrons	0.02	1.03
pions	$-0.10 + 0.0026 p$	$1.02 + 0.0004 p$

Table 5.2: Correction factors for $N_{dE/dx}^\sigma$

$N_{dE/dx}^\sigma$: The dE/dx ¹, the energy loss of a charged particle, and its error $\sigma_{dE/dx}$ (see eq. 3.1), are used to create a normalised $N_{dE/dx}^\sigma$ expression, defined as

$$N_{dE/dx}^\sigma = \frac{(dE/dx)_{meas} - (dE/dx)_{exp}}{S \times \sigma_{dE/dx}} \quad (5.1)$$

where S is a scale factor, $(dE/dx)_{meas}$ is the measured dE/dx value, and $(dE/dx)_{exp}$ is the expected value. The $N_{dE/dx}^\sigma$ distribution will have a mean of zero and a width of one. This allows one to make a simple momentum-independent requirement.

The values for $(dE/dx)_{corr} = 9.95 - (dE/dx)_{exp}$ and the S-factor were determined from control samples of electrons and pions which were created from the tau pair data and Monte Carlo. Note that the S-factor and $(dE/dx)_{corr}$ are evaluated for both electrons and pions with the Monte Carlo. The $(dE/dx)_{corr}$ and S-factors are given in Table 5.2. In Fig. 5.3 $N_{dE/dx}^\sigma$ is plotted for jets that pass the electron selection, except for the $N_{dE/dx}^\sigma$ requirement. It can be seen that removing events with $N_{dE/dx}^\sigma < -3$ will reduce much of the background while keeping a majority of the electron candidates.

¹in units of keV/cm

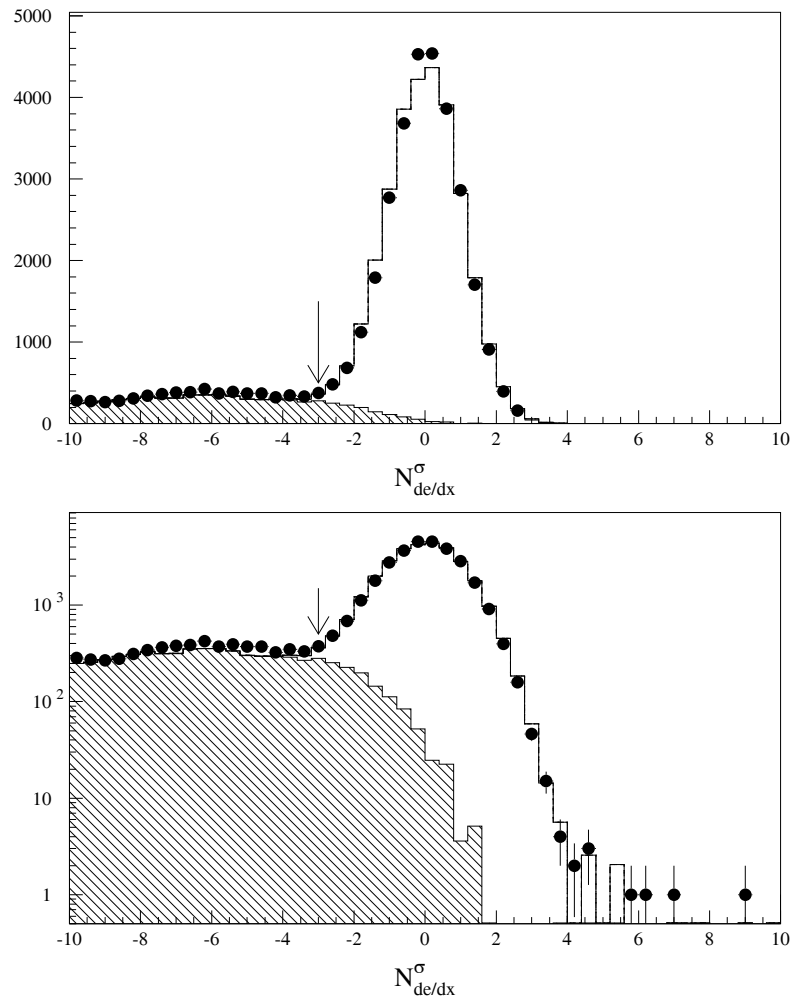


Figure 5.3: The value of $N_{dE/dx}^\sigma$ is plotted both linearly and logarithmically for data (solid points) and Monte Carlo (open histogram) passing the other electron selection requirements. The hatched histogram represents the Monte Carlo prediction for the background and the arrow indicates where the selection cut was applied.

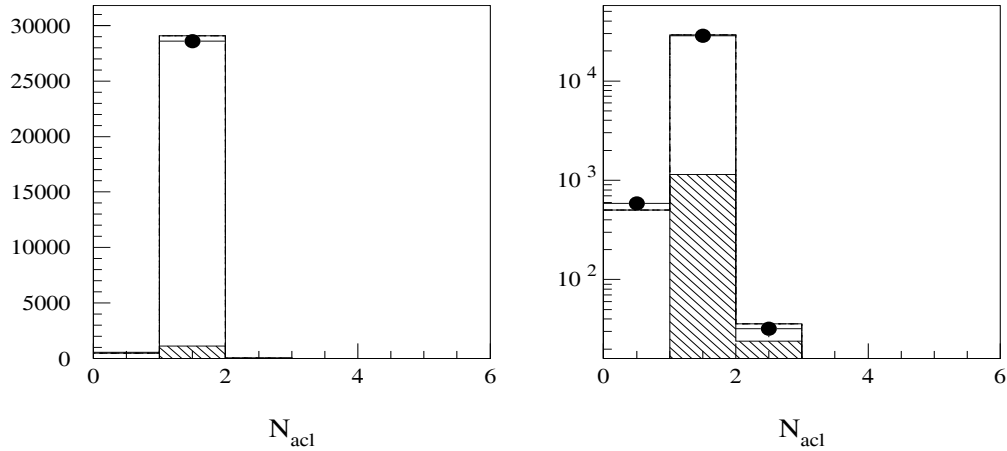


Figure 5.4: The number of clusters associated to a track, N_{acl} , passing all of the other electron selection cuts is plotted both linearly and logarithmically. The points are the data, the open histogram is the Monte Carlo prediction for the $\tau^- \rightarrow e^- \bar{\nu}_e \nu_\tau$ decays, and the hatched histogram is the Monte Carlo prediction for the background.

Cluster Requirements

This analysis uses a clustering algorithm optimised for τ decays [32]. Clusters are limited to a maximum of four EB blocks in a 2×2 configuration in (θ, ϕ) . The clusters are associated to the tracks using χ^2 -type parameters defined as

$$\chi_\theta^2 = \frac{(\theta_{track} - \theta_{cluster})^2}{\sigma_\theta^2}$$

$$\chi_\phi^2 = \frac{(\phi_{track} - \phi_{cluster})^2}{\sigma_\phi^2}$$

where $(\theta_{track}, \phi_{track})$ and $(\theta_{cluster}, \phi_{cluster})$ are respectively the extrapolated track and cluster positions at the ECAL; σ_θ and σ_ϕ are approximately 9 mr and include both the track and cluster uncertainties. A cluster is considered to be associated to a track if it satisfies $\chi_\theta^2 < 8$ and $\chi_\phi^2 < 8$.

The variable N_{acl} is the number of clusters associated to the primary track. In Fig. 5.4, the number of clusters associated to the primary track is plotted for jets that pass the electron selection. Tracks with $N_{acl} \geq 2$ are rejected.

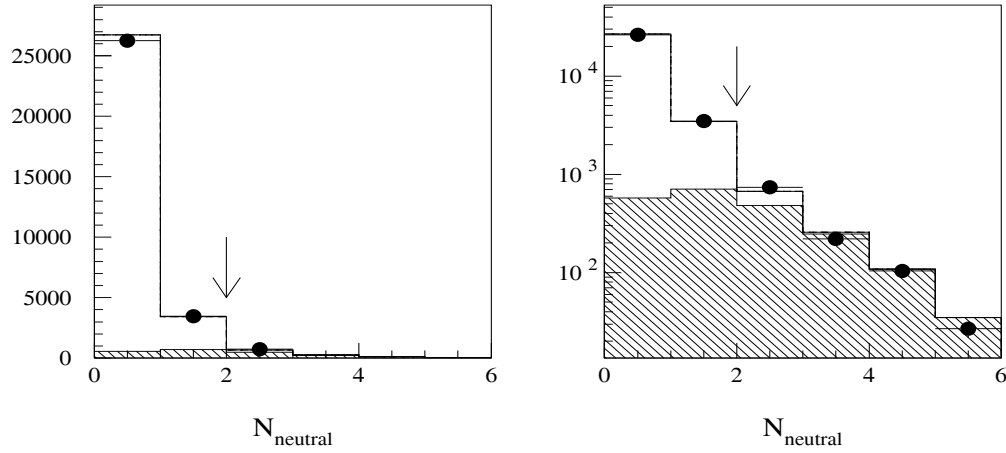


Figure 5.5: The number of neutral clusters passing all of the other electron selection cuts is plotted both linearly and logarithmically. The points are the data, the open histogram is the Monte Carlo prediction for the $\tau^- \rightarrow e^- \bar{\nu}_e \nu_\tau$ decays, the hatched histogram is the Monte Carlo prediction for the background and the arrow indicates where the selection cut is applied.

The variable $N_{neutral}$ is the number of neutral clusters in the jet, as shown in Fig. 5.5. Up to one neutral cluster is allowed into the sample.

E/p and $N_{E/p}^\sigma$

The E/p variable, the energy of the associated ECAL cluster divided by the primary track momentum, is used in two different ways, depending on whether the track momentum is above or below 5 GeV. There is little background after a dE/dx requirement for events with track momentum less than 5 GeV, as can be seen in the plots on the left hand side of Fig. 5.6. Therefore only a loose requirement of $E/p \geq 0.3$ is applied for those events.

The normalised E/p variable, $N_{E/p}^\sigma$, is used for tracks with $p \geq 5$ GeV and is defined

$ \cos\theta $	A	B	C	D	E
0-0.25	1.0069	-0.2075	0.0620	-0.055	0.133
0.25-0.50	1.0027	-0.2815	0.0530	-0.027	0.188
0.50-0.72	0.9881	-0.3046	0.0472	0.043	0.195

Table 5.3: Parameters for $N_{E/p}^\sigma$

as

$$N_{E/p}^\sigma = \frac{(E/p)_{meas} - (E/p)_{expected}}{\sigma_{E/p}}$$

where $(E/p)_{meas}$ is the measured E/p value and $\sigma_{E/p}$ is uncertainty on $(E/p)_{meas}$. As mentioned earlier, the normalised variable is independent of momentum so a simple requirement can be applied. The variables $(E/p)_{expected}$ are determined from control samples of electrons created by applying tight criteria to the tau data sample [33] and then by fitting the E/p distributions with gaussians for ten momentum bins and three $|\cos\theta|$ bins. For each $|\cos\theta|$ bin, the mean could be described by a function of the form

$$(E/p)_{expected} = A + \frac{B}{p},$$

while the width could be described by a function of the form

$$\sigma_{E/p} = C + \frac{D}{\sqrt{p}} + \frac{E}{p}.$$

The results of the fits obtained from reference [33] are displayed in Table 5.3. Table 5.4 includes the correction factors for electrons in the Monte Carlo. The $\mu_{E/p}^{MC}$ factor is added to $(E/p)_{expected}$ and the $\sigma_{E/p}^{MC}$ factor is divided into $\sigma_{E/p}$. In the right plots of Fig. 5.6, the $N_{E/p}^\sigma$ variable is plotted for the nominal electron selection for tracks with $p \geq 5$ GeV, and it can be seen that a cut at $N_{E/p}^\sigma \geq -3.5$ will keep most of the electron candidates while removing most of the background.

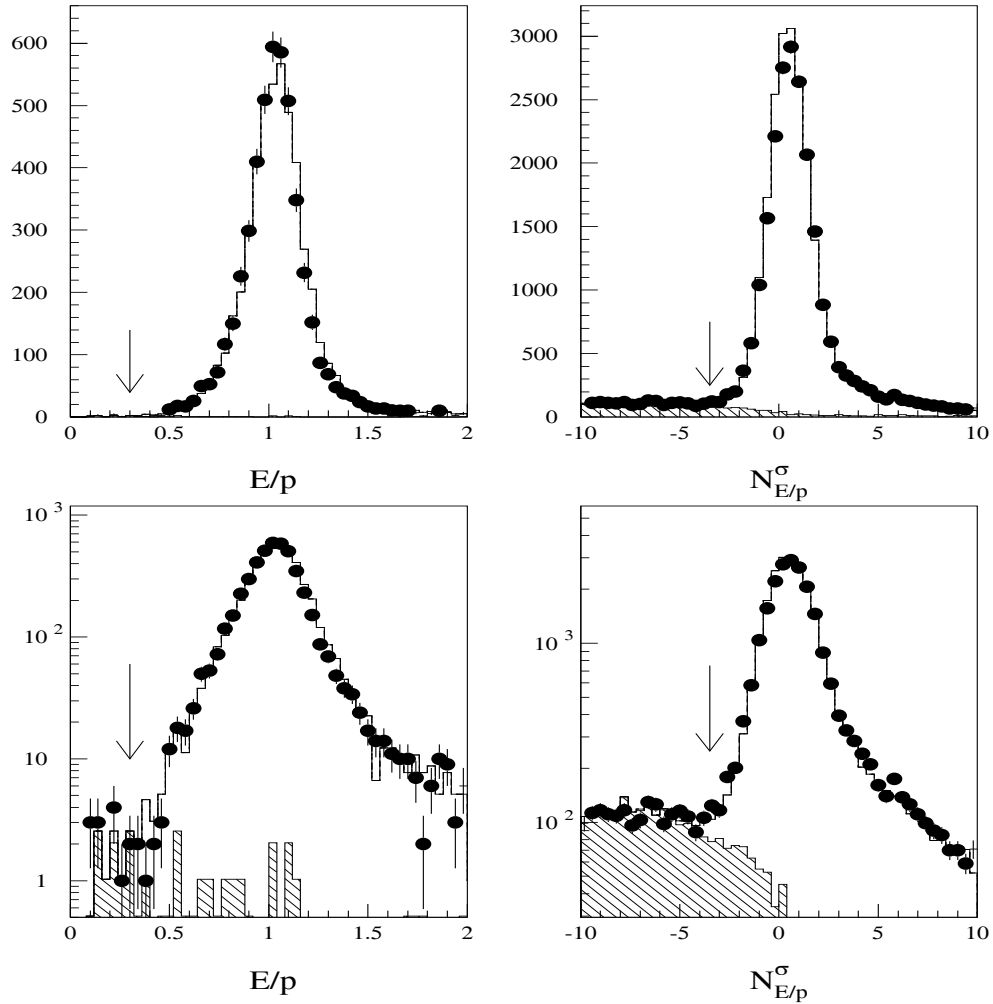


Figure 5.6: The plots on the left side show the variable E/p for $p < 5$ GeV (excluding the requirement in question), while the plots on the right side show the variable $N_{E/p}^{\sigma}$ both linearly and logarithmically. The points are the data, the open histogram is the Monte Carlo prediction for the $\tau^- \rightarrow e^- \bar{\nu}_e \nu_{\tau}$ decays, the hatched histogram is the Monte Carlo prediction for the background and the arrows indicate where the selection cut was applied.

$ \cos\theta $	$\mu_{E/p}^{MC}$	$\sigma_{E/p}^{MC}$
0-0.25	0.0047	0.864
0.25-0.50	0.0065	0.890
0.50-0.72	0.0072	0.965

Table 5.4: Monte Carlo Correction Factors for Electrons

Hadron Calorimeter Requirements

It is highly unlikely that an electron will reach the hadron calorimeter (HCAL) since there are ~ 26.5 radiation lengths of material in front of it. To make use of this fact, a quantity N_{layers}^{HCAL} is defined to be the number of HCAL layers (up to 9 layers) containing a signal.

The response of the HCAL to electrons and hadrons is not well modelled by the Monte Carlo, hence corrections must be made to it. Compared to an electron control sample created by applying tight criteria to the tau data sample, it was found that the number of electrons that penetrate into the HCAL must be increased in the Monte Carlo. This is done by increasing N_{layers}^{HCAL} by one for a small fraction of events. In Table 5.5 the first column gives the fraction of electrons that have one layer added. The hadron correction was slightly more complicated and two corrections were employed. The first takes the hadrons that do not reach the HCAL, and adds between 1-5 layers (randomly and with equal probability) to some fraction of the tracks in the Monte Carlo; these values are in the second column of Table 5.5. For hadrons that reach the HCAL, the Monte Carlo gives a smaller mean number of layers than the data, so the number of HCAL layers for randomly selected jets in the Monte Carlo is corrected by adding a factor based upon a Poisson probability function. The values for the means used for this correction are shown in the third column of Table 5.5. In Fig. 5.7 the uncorrected N_{layers}^{HCAL} is plotted on the left hand side. The corrected N_{layers}^{HCAL} is plotted on the right hand side of Fig. 5.7.

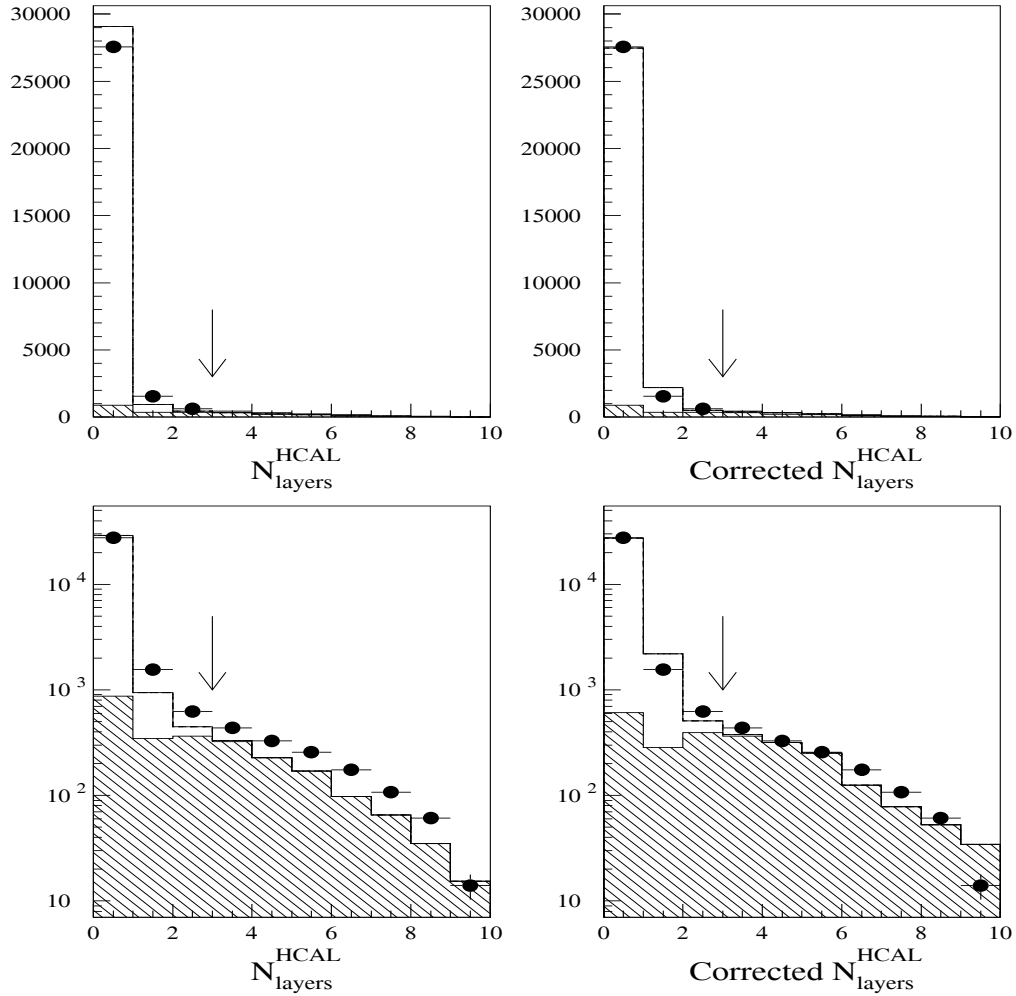


Figure 5.7: N_{layers}^{HCAL} is plotted before (left side) and after (right side) corrections are applied for jets passing all of the other electron selection cuts. N_{layers}^{HCAL} is plotted both linearly and logarithmically. The points are the data, the open histogram is the Monte Carlo prediction for the $\tau^- \rightarrow e^- \bar{\nu}_e \nu_\tau$ decays, the hatched histogram is the Monte Carlo prediction for the background and the arrow indicates where the selection cut is applied.

p range	e Fraction	h Fraction	h Mean
0-10	0.035	0.24	0.40
10-20	0.065	0.30	0.35
20-30	0.043	0.35	0.55
> 30	0.050	0.30	0.55

Table 5.5: Correction factors for N_{layers}^{HCAL}

Bhabha Rejection Requirements

The variable $\theta_{acoplanarity}$ is defined for this analysis as the angle between the primary track in one jet and the primary track in the opposite jet, calculated in the plane transverse to the beam direction. Tau events have at least two neutrinos per event and so $\theta_{acoplanarity}$ is a broad distribution. However $e^+e^- \rightarrow e^+e^-$ events, a background in the tau pair sample, tend to have a small $\theta_{acoplanarity}$ for high momentum tracks. In Fig. 5.8, $\theta_{acoplanarity}$ is plotted for events selected by the electron selection. In addition we require that the primary track has $p \geq 30$ GeV and the momentum of the primary track in the opposite hemisphere satisfies $p \geq 0.75E_{beam}$. The Monte Carlo does not include bhabha events and so a clear excess of data with low $\theta_{acoplanarity}$ is observed in the plot. Therefore jets with high momentum and $\theta_{acoplanarity} < 0.1^\circ$ are removed from the sample to suppress the bhabhas.

5.2.2 Photon Conversions

In addition to requirements listed in Table 5.1 for the dominant $\tau^- \rightarrow e^- \bar{\nu}_e \nu_\tau$ decay topology, there are additional requirements applied to jets with 2 or 3 tracks (see Table 5.6). Photons may be present in $\tau^- \rightarrow e^- \bar{\nu}_e \nu_\tau$ decays. One source of photons is from final state radiation where the tau emits a photon. Another source is from bremsstrahlung photons that are created as the electron passes through the material in the detector. Photons have a probability of approximately 3% of converting to an e^+e^- pair due to the material in the detector. Consequently there are $\tau^- \rightarrow e^- \bar{\nu}_e \nu_\tau$ decays with one or two extra charged

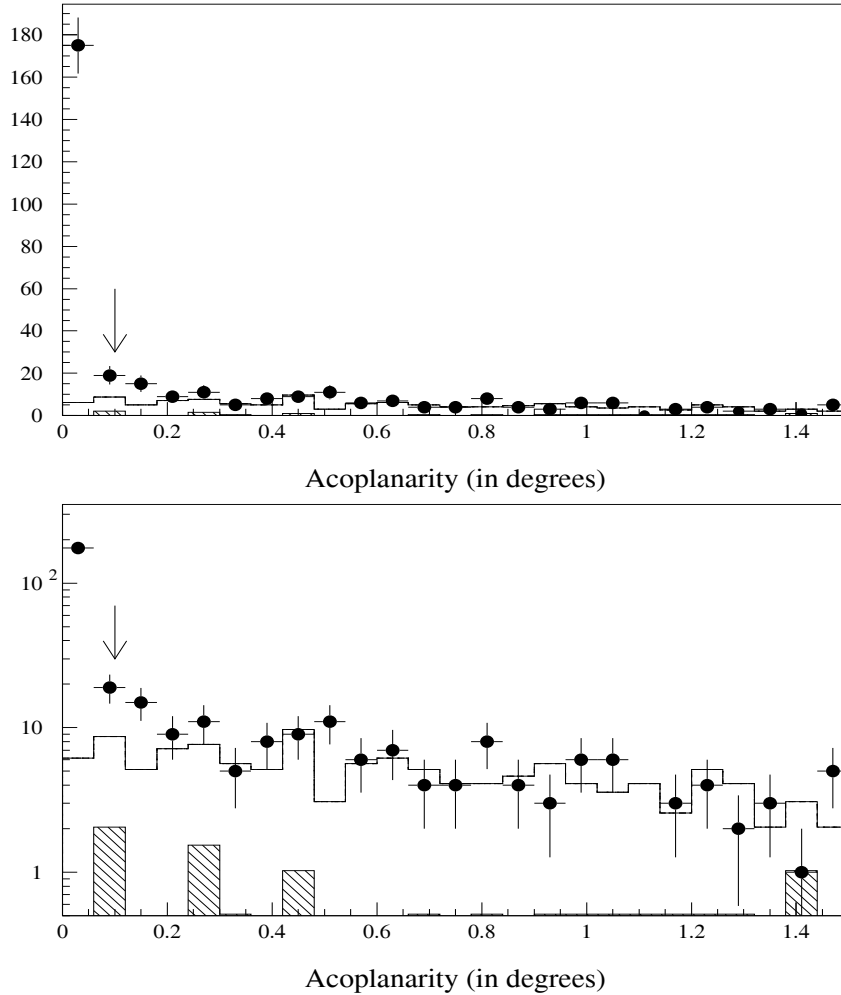


Figure 5.8: The acoplanarity angle for events selected by the nominal electron selection, where the track has momentum $p \geq 30$ GeV and the track in the opposite hemisphere has $p \geq 0.75E_{beam}$ is plotted linearly and logarithmically. The points are the data, the open histogram is the Monte Carlo prediction for the $\tau^- \rightarrow e^- \bar{\nu}_e \nu_\tau$ decays and the hatched histogram is the Monte Carlo prediction for the background and the arrow indicates where the selection cut was applied.

N_{tracks}	Requirements	Description
2	$p_2 \leq 3 \text{ GeV}$	p_2 : Momentum of track #2.
2	$N_{dE/dx}^\sigma(2) \geq -3$	$N_{dE/dx}^\sigma(2)$: Normalised value of dE/dx for track #2.
3	$p_2 + p_3 \leq 5 \text{ GeV}$	p_2 & p_3 : Momentum of track #2 and #3 resp.
3	$N_{dE/dx}^\sigma(2) \geq -3$	$N_{dE/dx}^\sigma(2)$: Normalised value of dE/dx for track #2.
3	$N_{dE/dx}^\sigma(3) \geq -3$	$N_{dE/dx}^\sigma(3)$: Normalised value of dE/dx for track #3.
3	$M_{23}^2 \leq 0.01 \text{ GeV}$	M_{23}^2 : Squared invariant photon mass.

Table 5.6: Extra Requirements for photon conversions

tracks. Both the e^+ and e^- tracks are observed in about 45% of these events, while for the remaining events one track is lost in the detector. Additional requirements for photon conversions are applied to the momenta, dE/dx and the mass of the second and third tracks. Fig. 5.9 shows the momentum and $N_{dE/dx}^\sigma$ for these second and third tracks in 2 and 3 track jets, as well as M_{23}^2 , the squared invariant mass of the second and third tracks from the photon conversion. Approximately 1.5% of the final $\tau^- \rightarrow e^- \bar{\nu}_e \nu_\tau$ sample contains jets with 2 or 3 tracks.

5.2.3 $\tau^- \rightarrow e^- \bar{\nu}_e \nu_\tau$ Decays With No Associated Cluster

The fourth $\tau^- \rightarrow e^- \bar{\nu}_e \nu_\tau$ decay topology, one in which the primary track has no associated cluster, can be detected by using the selection requirements listed in Table 5.1, with the exception of the E/p requirements. In addition to those requirements, the momentum of the primary track cannot exceed 5 GeV. The E/p requirements are not required because the primary track is either too low in momentum to reach the ECAL (bends back toward the vertex) or not energetic enough to penetrate the magnetic coil located in front of the ECAL. Approximately 3% of the final $\tau^- \rightarrow e^- \bar{\nu}_e \nu_\tau$ sample are electron candidates that have no associated cluster in the ECAL.

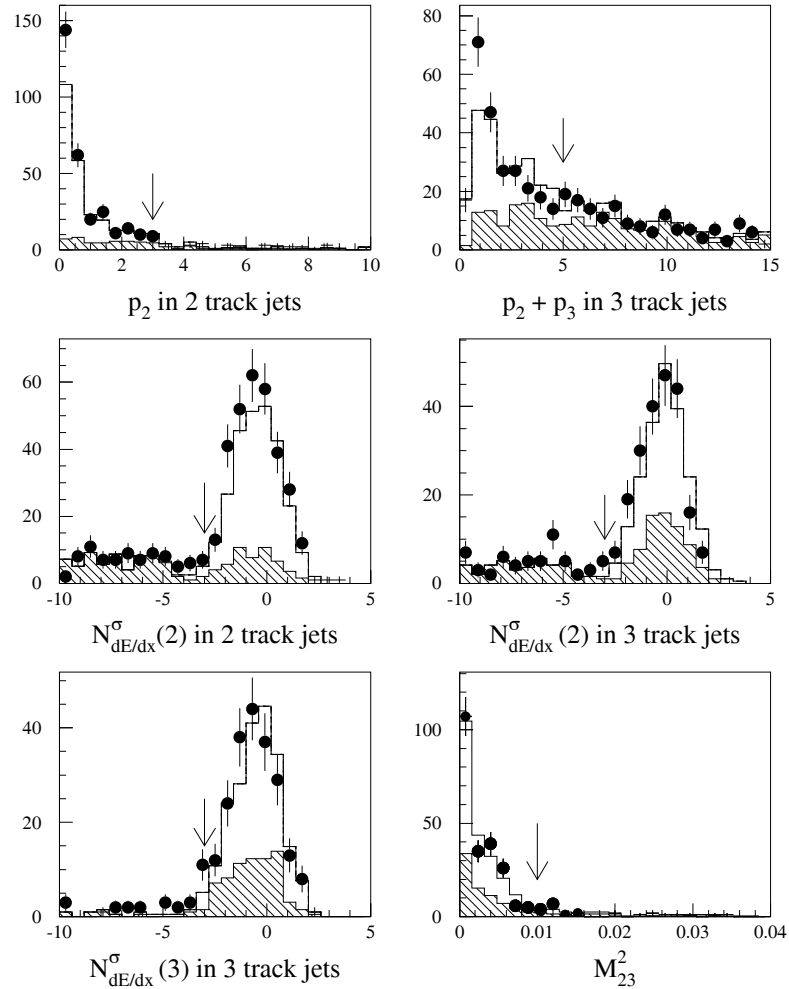


Figure 5.9: The momenta and the variable $N_{dE/dx}^\sigma$ are shown for the second track in 2 track jets for events that pass all of the other electron selection cuts. The sum of the momenta and the $N_{dE/dx}^\sigma$ are shown for the second and third tracks for 3 track jets. The last plot gives the squared invariant mass of the second and third tracks in 3 track jets. The points are the data, the open histogram is the Monte Carlo prediction for the $\tau^- \rightarrow e^- \bar{\nu}_e \nu_\tau$ decays, the hatched histogram is Monte Carlo prediction for the background, and the arrows indicate where the electron selection cut was made for that particular variable.

Requirements	Description
$N_{CJ}^{hits}(1) + N_{CJ}^{hits}(2) < 200$	N_{CJ}^{hits} : No. of CJ hits for tracks #1 and #2.
$6.5^\circ < mod(\phi, 15) < 8.5^\circ$	ϕ : Angle of track position.

Table 5.7: Extra Requirements for split track jets

5.2.4 Split Tracks

The final $\tau^- \rightarrow e^- \bar{\nu}_e \nu_\tau$ decay topology examined in this analysis is the *split track* case. A split track is defined as a single charged track that is reconstructed as two tracks, see Table 5.7 for split track requirements. This occurs when the track passes close to one of the anode planes of the jet chamber (see Fig. 3.3). The signals on the wires are sensitive to field effects and the position resolution is degraded as a particle passes very close to an anode plane. Split tracks generally have hits on both sides of the anode plane, but as the track crosses the anode plane a discontinuity arises splitting the track into two, thus causing the tracking software to reconstruct two tracks in the jet.

Fig. 5.10(a) shows the number of *CJ* hits for the primary and secondary tracks for all 2-track jets, it shows that a peak occurs around 160 in the data while no such peak occurs in the Monte Carlo. Thus it is required in the selection that if any 2-track jets have a *CJ* hit sum of less than 200, these particles will be kept, pending further cuts. Note that those 2-track jets with more than 200 hits are assumed to be photon conversions. The Jet Chamber has 24 sectors with 15° separating the cathode planes. In Fig. 5.10(b) the position of a track with a given sector, $mod(\phi, 15^\circ)$, is shown for events with $N_{CJ}^{hits}(1) + N_{CJ}^{hits}(2) < 200$. To keep the data with tracks near the anode plane, a cut is applied on either side of the peak in this plot. The track with the highest number of *CJ* hits will be kept as the electron candidate. There are 362 split track candidates in the tau data sample. After being identified as a split track candidate, the particle must then pass the electron selection requirements for the dominant $\tau^- \rightarrow e^- \bar{\nu}_e \nu_\tau$ decay topology, with or without an associated cluster in the electromagnetic calorimeter. Approximately 0.1% of the final $\tau^- \rightarrow e^- \bar{\nu}_e \nu_\tau$ sample are identified as split track jets.

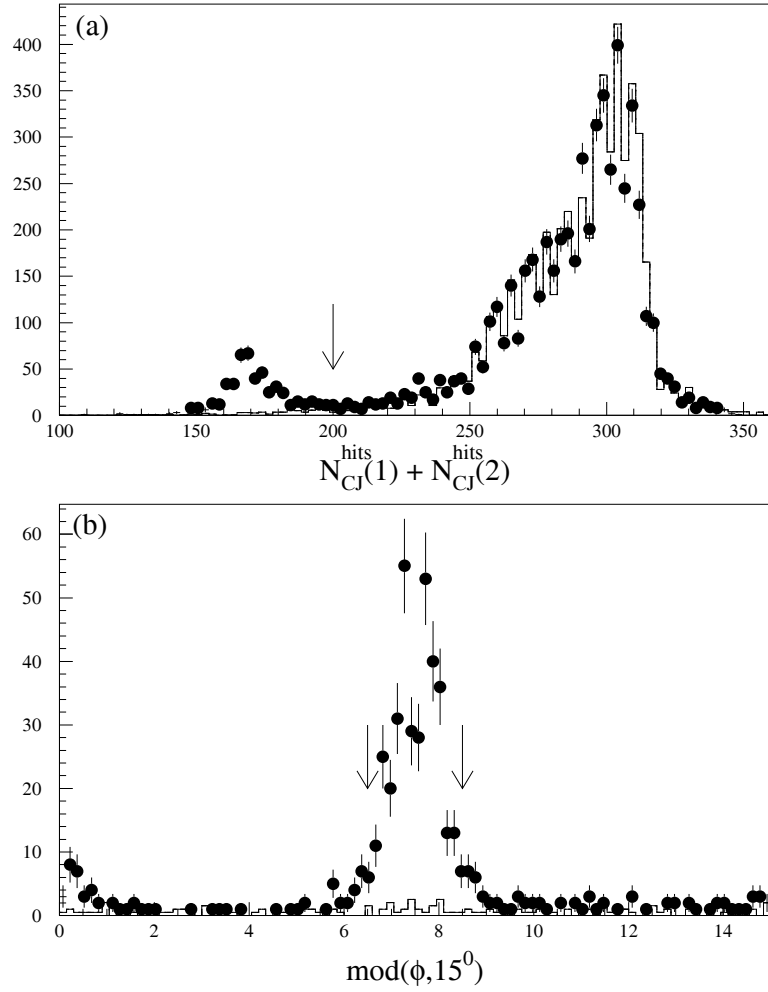


Figure 5.10: (a) The number of CJ hits added together for all two track jets in the tau-pair data ($N_{CJ}^{hits}(1) + N_{CJ}^{hits}(2)$), where split track candidates have $N_{CJ}^{hits}(1) + N_{CJ}^{hits}(2) < 200$. (b) The $\text{mod}(\phi, 15^\circ)$ for two track jets and $N_{CJ}^{hits}(1) + N_{CJ}^{hits}(2) < 200$. As can be seen the Monte Carlo does not model the data near the anode plane ($\text{mod}(\phi, 15^\circ) = 7.5^\circ$); the data between the arrows are the split track candidates and are kept for further analysis. For both plots the points are the data and the open histogram is the tau Monte Carlo.

5.3 Electron Selection Results

After the $\tau^- \rightarrow e^- \bar{\nu}_e \nu_\tau$ selection as outlined in this chapter, a total of 29738 $\tau^- \rightarrow e^- \bar{\nu}_e \nu_\tau$ candidates, including photon conversions and split track candidates, were selected out of the 166948 taus identified by the tau-pair selection.

The overall $\tau^- \rightarrow e^- \bar{\nu}_e \nu_\tau$ selection efficiency for the requirements listed in the previous section is calculated to be $(96.13 \pm 0.10)\%$. This efficiency was obtained from studying the Monte Carlo. The efficiency for the ECAL geometry and $N_{dE/dx}^{hits}$ requirements were checked by using tau-pair data samples. The efficiency found for the ECAL geometry requirement using the data sample, 0.9891 ± 0.0003 , was in good agreement with the Monte Carlo sample, 0.9899 ± 0.0002 , consequently no correction was applied. The efficiency for the $N_{dE/dx}^{hits}$ requirement obtained from the data sample, 0.9930 ± 0.0003 , was found to differ slightly from the Monte Carlo efficiency, 0.9946 ± 0.0002 . This difference was found to be dependent on the momentum of the particle. As a result a momentum dependent correction was applied to the overall selection efficiency.

Chapter 6

Background Analysis

This chapter discusses the background in the electron sample. The largest background in the electron sample is from hadronic tau decays: $\tau^- \rightarrow h^- \nu_\tau$ and $\tau^- \rightarrow h^- \geq 1\pi^0 \nu_\tau$, where h^- is either a π^- or a K^- . Hadrons remain in the electron sample for a number of reasons. The dE/dx of high momentum electrons and hadrons is nearly identical. In addition the loose requirement on the number of HCAL layers allows hadrons to enter the sample. Hadrons accompanied by π^0 's can have an E/p value similar to an electron if the two photons from the π^0 decay overlap the associated cluster.

There are also contributions from the $e^+e^- \rightarrow e^+e^-$ and $e^+e^- \rightarrow (e^+e^-)e^+e^-$ reactions. The $e^+e^- \rightarrow e^+e^-$ background remains because an electron emitting a photon can cause the resulting track to have a larger $\theta_{acoplanarity}$ angle. There are no requirements in the electron selection to remove low energy $e^+e^- \rightarrow (e^+e^-)e^+e^-$ background events.

The backgrounds in the electron sample are given in Table 6.1. The backgrounds were estimated using Monte Carlo samples. The modelling of each of the backgrounds by the Monte Carlo was checked by creating subsamples from the electron candidates enriched in the background. We calculate a correction factor,

$$C_{bkgd} = \frac{N_{data} - N_{MC-other}}{N_{MC-bkgd}}, \quad (6.1)$$

where $N_{MC-bkgd} = N_{MC} - N_{MC-other}$ are the enhanced background events, N_{data} are the integrated numbers of events from the data sample, and $N_{MC-other}$ are the other Monte Carlo background events that are also present. The numbers of events are obtained from a

Channel	Monte Carlo Background	Corrected Background
$\tau^- \rightarrow h^- \geq 1\pi^0\nu_\tau$	0.0303 ± 0.0007	0.0310 ± 0.0019
$\tau^- \rightarrow h^- \nu_\tau$	0.0098 ± 0.0004	0.0103 ± 0.0015
other τ decays	0.0022 ± 0.0002	0.0022 ± 0.0006
$e^+e^- \rightarrow e^+e^-$	0.0044 ± 0.0003	0.0057 ± 0.0012
$e^+e^- \rightarrow (e^+e^-)e^+e^-$	0.0054 ± 0.0003	0.0054 ± 0.0015
Total	0.0456 ± 0.0012	0.0546 ± 0.0031

Table 6.1: The backgrounds in the $\tau^- \rightarrow e^- \bar{\nu}_e \nu_\tau$ sample. The numbers given are fractions of tau decays. The first column displays the fractions taken directly from the Monte Carlo while the second column displays the corrected fractions after the data and Monte Carlo have been compared.

reference distribution with the integration region chosen so that the statistical error on C_{bkgd} is minimised. The statistical error on C_{bkgd} is added to the uncertainty of the background estimate. The following sections will discuss the individual backgrounds.

6.1 $\tau^- \rightarrow h^- \geq 1\pi^0\nu_\tau$

The largest background in the electron sample is from tau decays to hadrons accompanied by any number of π^0 's. One third of these events have one π^0 with the remainder having two π^0 's.

The modelling of the $\tau^- \rightarrow h^- \geq 1\pi^0\nu_\tau$ background can be checked by examining the mass distribution for jets with one neutral cluster. The jet mass is calculated using track information for one four-vector, and cluster direction and energy for the second four-vector (we assume that both particles are pions). The invariant mass of the jet for electron candidates is shown in Fig. 6.1(a) when $N_{neutral} = 1$ and $p \geq 5$ GeV. The shaded part of the histogram is the electron contribution. The $p \geq 5$ GeV requirement is added as there is

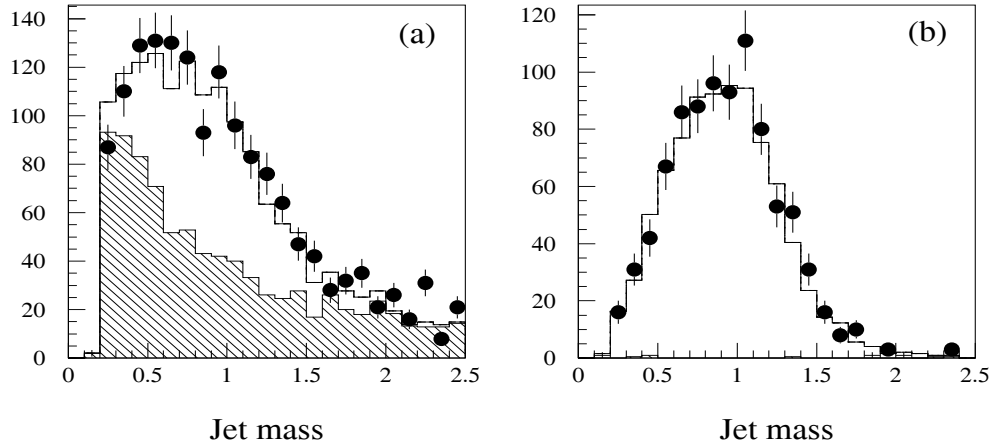


Figure 6.1: The left plot shows the jet mass for electron candidates with $N_{neutral} = 1$ and $p \geq 5$ GeV; the points are hadron candidates, the open histogram is the Monte Carlo prediction for hadrons and the hatched histogram is the electron contribution. The right plot shows a similar plot but with the $N_{dE/dx}^{\sigma}$ requirement reversed so that hadrons are selected.

no background in our electron sample in this region.

Fig. 6.1(b) shows the same quantity except that the requirement on $N_{dE/dx}^{\sigma}$ has been reversed so that it selects hadrons rather than electrons ($N_{dE/dx}^{\sigma} \leq -3.0$). The $\tau^- \rightarrow h^- \geq 1\pi^0\nu_{\tau}$ background will be estimated using Fig. 6.1(b). The number of hadrons in the data (N_{data}) are 894, the number of hadrons in the Monte Carlo ($N_{MC-bkgd}$) are 873 and there are 4 other Monte Carlo particles ($N_{MC-other}$), consequently $C_{bkgd} = 1.02 \pm 0.06$. Therefore the $\tau^- \rightarrow h^- \geq 1\pi^0\nu_{\tau}$ background is estimated to be 1.02 times the Monte Carlo background and 6% is added in quadrature to the uncertainty. Thus the $\tau^- \rightarrow h^- \geq 1\pi^0\nu_{\tau}$ background in the $\tau^- \rightarrow e^- \bar{\nu}_e \nu_{\tau}$ sample is 0.0310 ± 0.0019 .

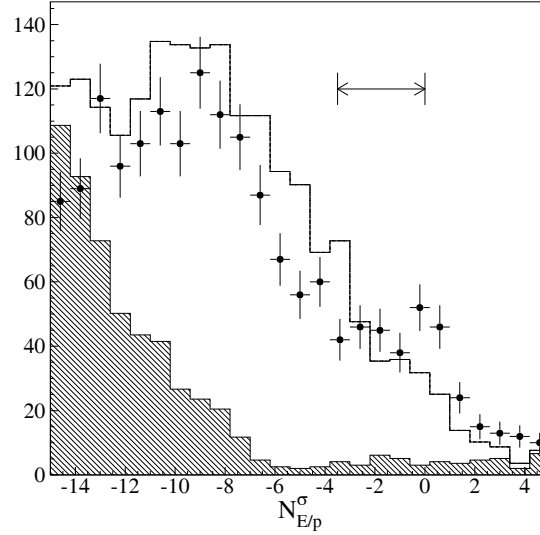


Figure 6.2: The normalised E/p variable, $N_{E/p}^{\sigma}$, for electron candidates with $N_{neutral} = 0$ and $p \geq 5$ GeV but with the $N_{dE/dx}^{\sigma}$ requirement reversed so that hadrons are selected. The unhatched part of the histogram is the $\tau^{-} \rightarrow h^{-}\nu_{\tau}$ contribution, while the hatched part is from hadrons accompanied by π^0 's.

6.2 $\tau^{-} \rightarrow h^{-}\nu_{\tau}$

A control sample of $\tau^{-} \rightarrow h^{-}\nu_{\tau}$ decays was created using the electron selection with $N_{neutral} = 0$ and $p \geq 5$ GeV, but with the $N_{dE/dx}^{\sigma}$ requirement reversed so that hadrons are selected. The normalised E/p variable, $N_{E/p}^{\sigma}$, for this control sample is shown in Fig. 6.2. The unshaded part of the histogram is the $\tau^{-} \rightarrow h^{-}\nu_{\tau}$ contribution, while the shaded part is from $\tau^{-} \rightarrow h^{-} \geq 1\pi^0\nu_{\tau}$ decays. The correction factor was calculated for the region $-3.5 \leq N_{E/p}^{\sigma} \leq 0.$, the lower bound of which corresponds to the lower bound of the electron selection. There were 193 $\tau^{-} \rightarrow h^{-}\nu_{\tau}$ candidates selected from the data (N_{data}), 185 $\tau^{-} \rightarrow h^{-}\nu_{\tau}$ selected from the Monte Carlo ($N_{MC-bkgd}$) and 19 $\tau^{-} \rightarrow h^{-} \geq 1\pi^0\nu_{\tau}$ candidates ($N_{MC-other}$). Therefore $C_{bkgd} = 1.04 \pm 0.15$. Consequently the $\tau^{-} \rightarrow h^{-}\nu_{\tau}$ background is scaled up by 4% and 15% is added in quadrature to the uncertainty. Thus the $\tau^{-} \rightarrow h^{-}\nu_{\tau}$ background in the $\tau^{-} \rightarrow e^{-}\bar{\nu}_e\nu_{\tau}$ sample is 0.0103 ± 0.0015 .

6.3 Other τ decay modes

The background from other tau decay modes is quite small. However, the uncertainty from these modes is scaled to three times the combined uncertainty from Monte Carlo statistics and the uncertainty in the Monte Carlo branching ratios. The uncertainty is conservatively increased by three because we do not check these backgrounds as we do for the other cases.

6.4 $e^+e^- \rightarrow e^+e^-$

A Monte Carlo sample of 197950 bhabha events was used for the $e^+e^- \rightarrow e^+e^-$ background analysis. The $e^+e^- \rightarrow e^+e^-$ events were passed through the tau-pair and $\tau^- \rightarrow e^- \bar{\nu}_e \nu_\tau$ selection algorithms and a total of 60 e^+e^- events remained. This bhabha sample corresponds to a luminosity of 47.5 pb^{-1} . Scaling the number of events to match the luminosity of the tau-pair Monte Carlo gives a $e^+e^- \rightarrow e^+e^-$ background of $0.0044 \pm 0.0003(\text{stat.})$ in the $\tau^- \rightarrow e^- \bar{\nu}_e \nu_\tau$ sample.

This background estimate can be verified by comparing distributions of data and Monte Carlo. The shower energy, $\Sigma E_{clus}/E_{beam}$, is plotted after the $\tau^- \rightarrow e^- \bar{\nu}_e \nu_\tau$ selection in Fig. 6.3(a), where ΣE_{clus} is the total ECAL cluster energy in the jet and E_{beam} is the beam energy. Fig. 6.3(b) shows an expanded view of the region where the $e^+e^- \rightarrow e^+e^-$ background is large. The points are the tau data, the open histogram is the combined $e^+e^- \rightarrow \tau^+\tau^-$ and $e^+e^- \rightarrow e^+e^-$ Monte Carlo and the hatched histogram is the $e^+e^- \rightarrow e^+e^-$ Monte Carlo. The predicted background fraction $e^+e^- \rightarrow e^+e^-$ in the $\tau^- \rightarrow e^- \bar{\nu}_e \nu_\tau$ sample is modified using the results illustrated in Fig. 6.3(b). There are 1638 taus (N_{data}), 220 $e^+e^- \rightarrow e^+e^-$ Monte Carlo ($N_{MC-bkgd}$) and 1349 tau Monte Carlo ($N_{MC-other}$) jets, consequently $C_{bkgd} = 1.31 \pm 0.26$. Hence the total $e^+e^- \rightarrow e^+e^-$ background in the $\tau^- \rightarrow e^- \bar{\nu}_e \nu_\tau$ sample is estimated to be 0.0057 ± 0.0012 .

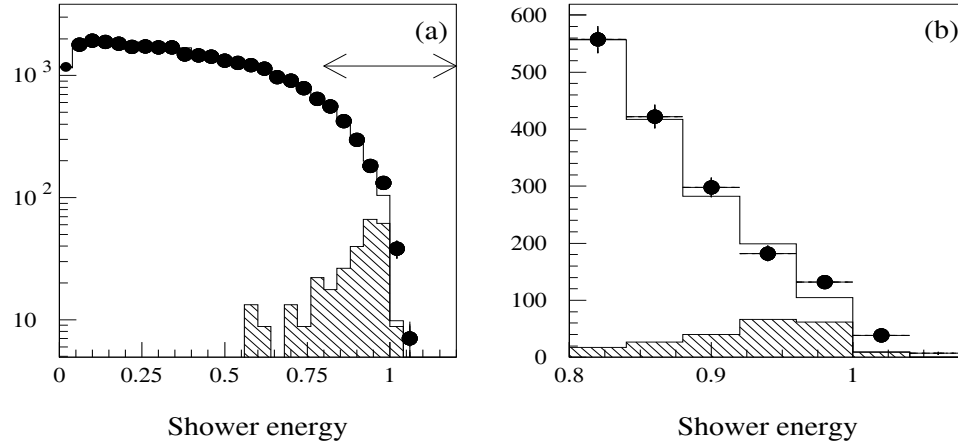


Figure 6.3: (a) The shower energy, $\Sigma E_{clus}/E_{beam}$ after the $\tau^- \rightarrow e^- \bar{\nu}_e \nu_\tau$ selection. (b) Expanded view of the shower energy. For both plots the histogram is the combined $e^+e^- \rightarrow \tau^+\tau^-$ and $e^+e^- \rightarrow e^+e^-$ Monte Carlo, the points are the data and the hatched histogram is the $e^+e^- \rightarrow e^+e^-$ background.

6.5 $e^+e^- \rightarrow (e^+e^-)e^+e^-$

A Monte Carlo sample of 186042 $e^+e^- \rightarrow (e^+e^-)e^+e^-$ events was used for the two-photon background analysis. Cuts are applied in the $\tau^- \rightarrow e^- \bar{\nu}_e \nu_\tau$ selection, such as the $\theta_{acoplanarity}$ requirement, that reduce the $e^+e^- \rightarrow e^+e^-$ background, however no cuts are applied to remove the $e^+e^- \rightarrow (e^+e^-)e^+e^-$ background. Thus almost all of those events that passed the tau selection also passed the electron selection, giving 269 $e^+e^- \rightarrow (e^+e^-)e^+e^-$ events. These events were then scaled to match the luminosity of the tau-pair Monte Carlo giving a $e^+e^- \rightarrow (e^+e^-)e^+e^-$ background of $0.0054 \pm 0.0003(stat.)$ in the $\tau^- \rightarrow e^- \bar{\nu}_e \nu_\tau$ candidate sample.

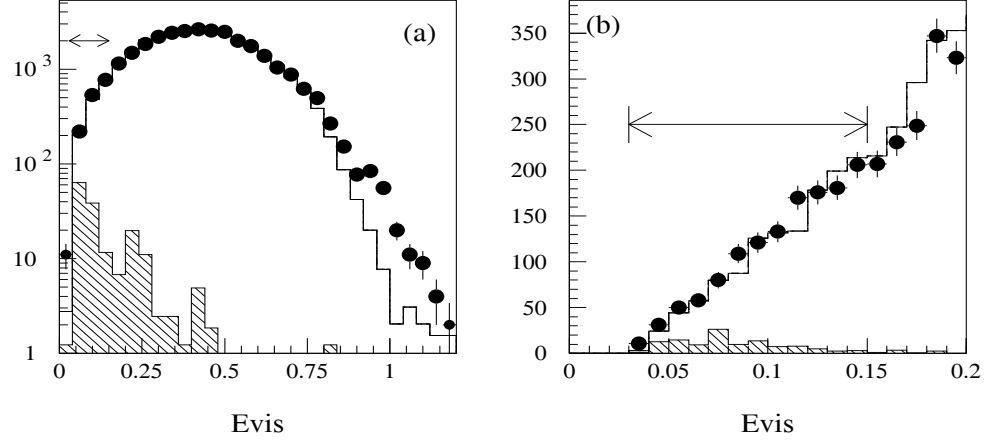


Figure 6.4: (a) The visible energy, $(\Sigma E_{clus} + \Sigma p_{track})/E_{CM}$ after the $\tau^- \rightarrow e^- \bar{\nu}_e \nu_\tau$ selection. (b) Expanded view of the visible energy. For both plots the histogram is the combined $e^+e^- \rightarrow \tau^+\tau^-$ and $e^+e^- \rightarrow (e^+e^-)e^+e^-$ Monte Carlo, the points are the data and the hatched histogram is the $e^+e^- \rightarrow (e^+e^-)e^+e^-$ Monte Carlo background.

This background estimate can be verified by comparing distributions of data and Monte Carlo. The visible energy, $(\Sigma E_{clus} + \Sigma p_{track})/E_{CM}$, is plotted after the $\tau^- \rightarrow e^- \bar{\nu}_e \nu_\tau$ selection in Fig. 6.4(a), where Σp_{track} is the total track momentum of the jet and E_{CM} is twice the beam energy. Fig. 6.4(b) shows an expanded view of the region where the $e^+e^- \rightarrow (e^+e^-)e^+e^-$ background is large. The open histogram is the combined $e^+e^- \rightarrow \tau^+\tau^-$ and $e^+e^- \rightarrow (e^+e^-)e^+e^-$ Monte Carlo, the points are the data and the hatched histogram is the $e^+e^- \rightarrow (e^+e^-)e^+e^-$ Monte Carlo background. In the region from 0.03 to 0.15 we observe 1326 jets in the data sample (N_{data}), 1165 tau Monte Carlo jets ($N_{MC-other}$) and 114 $e^+e^- \rightarrow (e^+e^-)e^+e^-$ Monte Carlo jets ($N_{MC-bkgd}$). This suggests that the $e^+e^- \rightarrow (e^+e^-)e^+e^-$ Monte Carlo is consistent with the data at the level of nearly 30% (*i.e.* $C_{bkgd} = 1.0 \pm 0.3$). Therefore the error on the background for $e^+e^- \rightarrow (e^+e^-)e^+e^-$ is scaled up by this amount, thus giving 0.0054 ± 0.0015 as the $e^+e^- \rightarrow (e^+e^-)e^+e^-$ background in the $\tau^- \rightarrow e^- \bar{\nu}_e \nu_\tau$ sample.

Chapter 7

Branching Ratio Determination

This chapter describes the measurement of the $\tau^- \rightarrow e^- \bar{\nu}_e \nu_\tau$ branching ratio. The first section gives the $\tau^- \rightarrow e^- \bar{\nu}_e \nu_\tau$ branching ratio result and the second section discusses the errors on the $\tau^- \rightarrow e^- \bar{\nu}_e \nu_\tau$ branching ratio.

7.1 Branching Ratio Results

Table 7.1 gives the results of this analysis used to calculate the branching ratio of the $\tau^- \rightarrow e^- \bar{\nu}_e \nu_\tau$ decay from equation (2.18). The result is

$$B(\tau^- \rightarrow e^- \bar{\nu}_e \nu_\tau) = 0.1778 \pm 0.0009 \pm 0.0011 ,$$

where the first error is statistical and the second is systematic. The statistical error is determined by propagating the binomial error on the number of events selected in the final sample. The estimated systematic errors discussed in more detail below are calculated from the errors on the backgrounds, efficiencies and the bias factor.

7.2 Systematic Errors

The breakdown of the systematic errors is given in Table 7.2. The uncertainty from the non-electron background was discussed in chapter 6. The uncertainty in the non-tau

N_{τ}^{sel}	166948
N_e^{sel}	29738
f_{bkgd}^e	0.0546 ± 0.0031
f_{bkgd}^{τ}	0.0183 ± 0.0030
ϵ_e	0.9613 ± 0.0010
F_{bias}^e	1.0036 ± 0.0022
$B(\tau^- \rightarrow e^- \bar{\nu}_e \nu_{\tau})$	$0.1778 \pm 0.0009 \pm 0.0011$

Table 7.1: Branching ratio data

Efficiency	$+0.00072$ -0.00051
Non-electron Background	0.00059
Non-tau background	0.00054
Bias factor	0.00039
Monte Carlo Statistics	0.00014
Photon conversions	0.00002
Total	0.0011

Table 7.2: Systematic Errors

background was taken from reference [31]. The uncertainty in the bias factor F_{bias}^e was taken from reference [34]. The uncertainty for the Monte Carlo Statistics is a quadratic combination of the statistical error on the selection efficiency, ϵ_e^{ES} , and the uncertainties on the correction factors due the electromagnetic calorimeter geometry requirements and the $N_{dE/dx}^{hits}$ requirements. The photon conversion and efficiency systematic errors will be discussed in greater detail below.

7.2.1 Photon Conversion Uncertainty

The probability for a photon converting to an e^+e^- pair depends critically on the amount of material the photon passes through. The Monte Carlo includes our best knowledge of the detector material but it is impossible to know this precisely. If the Monte Carlo conversion probability is different than the real conversion probability, then the efficiency may not be correct.

As a systematic check we artificially raise and lower the photon conversion probability in the Monte Carlo by $\pm 10\%$. This is done by re-weighting the events and then calculating the efficiency. The branching ratio was re-calculated for both cases and observed to change by ± 0.0002 . The small change is not unexpected as we accept jets with up to 3 charged tracks. Changing the photon conversion probability just shifts the data within the sample.

7.2.2 Electron Selection Efficiency

The uncertainty in the efficiency of the electron selection is evaluated separately for each variable used in the selection. To determine the errors on the branching ratio the variable in question is varied above and below the best cut value, while all the other variables remain the same. The individual systematic error bounds determined for each variable are shown in Table 7.3.

The ranges that each variable was changed to determine the systematic error bounds are shown in the second column of Table 7.3. Figs. 7.1 and 7.2 show the variation in the branching ratio for the electron selection requirements listed in Table 7.3. The solid line is the $\tau^- \rightarrow e^- \bar{\nu}_e \nu_\tau$ branching ratio using the regular electron selection requirements. The error bars are calculated from the quadratic difference between the different cut values and the $\tau^- \rightarrow e^- \bar{\nu}_e \nu_\tau$ branching ratio using the nominal cut values.

The systematic errors from Table 7.3 are summed in quadrature, giving a total systematic error for the electron selection efficiency of $^{+0.00072}_{-0.00051}$.

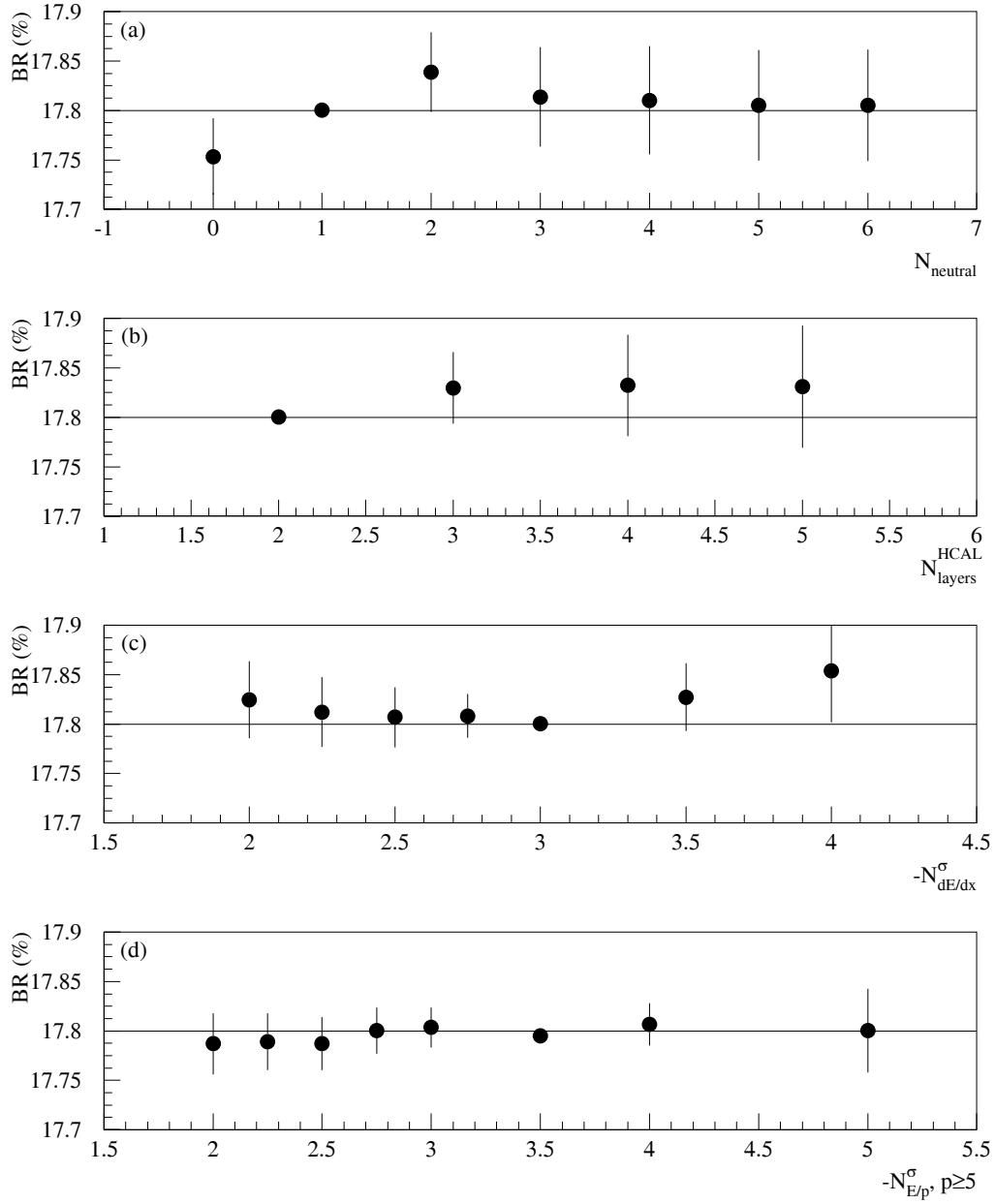


Figure 7.1: The $\tau^- \rightarrow e^- \bar{\nu}_e \nu_\tau$ branching ratio versus different cut values. The points are the branching ratio values, including the relative systematic errors between the different cut values and the best cut value. The solid line is the electron branching ratio.

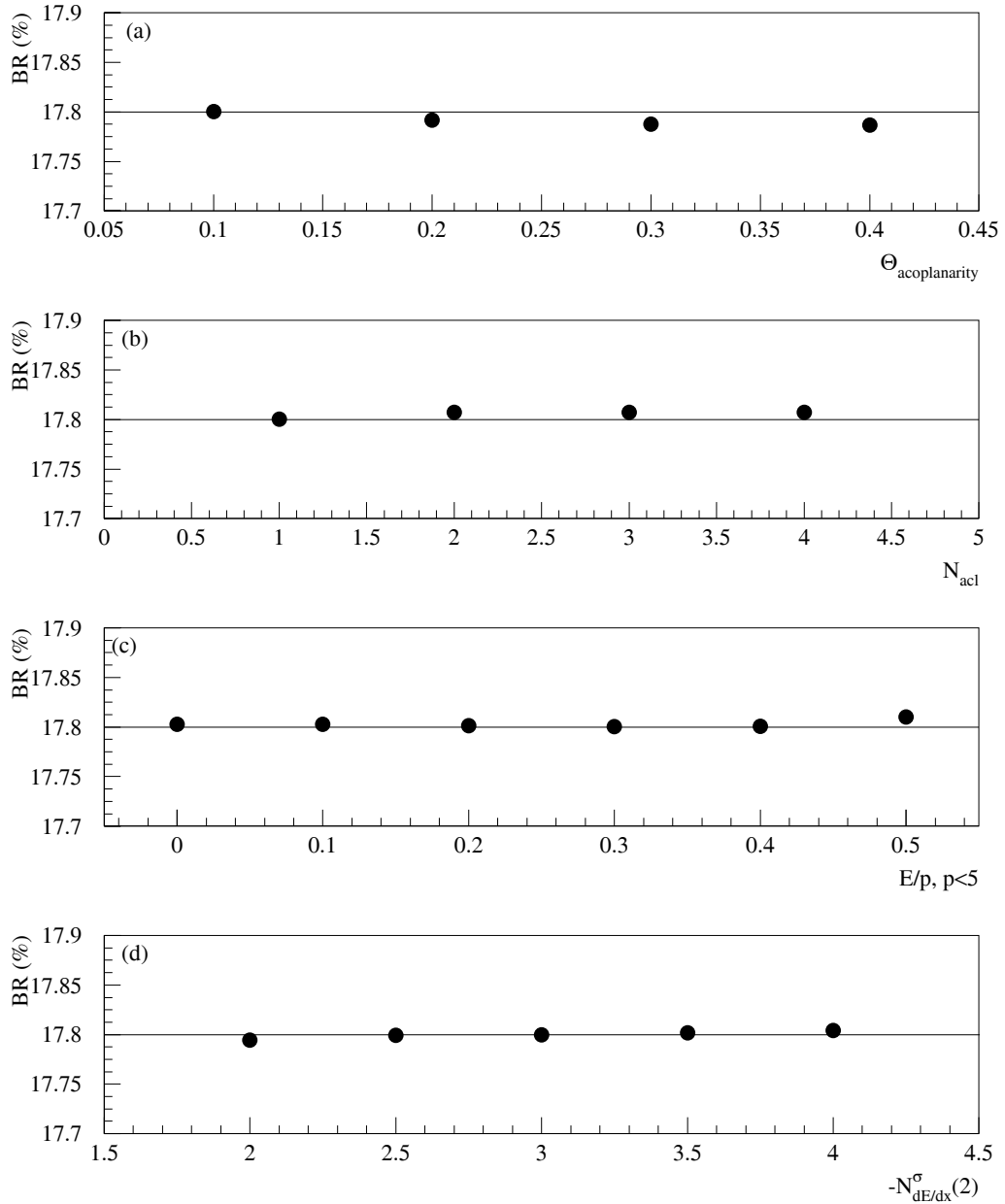


Figure 7.2: The $\tau^- \rightarrow e^- \bar{\nu}_e \nu_\tau$ branching ratio versus different cut values. The points are the branching ratio values, including the relative systematic errors between the different cut values and the best cut value. The solid line is the electron branching ratio. Note that the error bars are smaller than the data points in all four plots.

Variable	Range varied	δB^-	δB^+
$N_{neutral}$	0 to 6	0.00047	0.00038
N_{layers}^{HCAL}	2 to 5	0	0.00032
$N_{dE/dx}^\sigma$	-2 to -4	0	0.00053
$N_{E/p, p \geq 5}^\sigma$	-2 to -5	0.00014	0.00007
$\theta_{acoplanarity}$	0.1° to 0.4°	0.00014	0
N_{acl}	0 to 4	0	0.00007
$E/p, p < 5$	0 to 0.4	0	0.00010
$N_{dE/dx}^\sigma(2)$	-2 to -4	0.00006	0.00004
Total		0.00051	0.00072

Table 7.3: Efficiency Systematic Errors

Chapter 8

Discussion of Results

This first section of this chapter compares the $\tau^- \rightarrow e^- \bar{\nu}_e \nu_\tau$ branching ratio result with $\tau^- \rightarrow e^- \bar{\nu}_e \nu_\tau$ branching ratio measurements from other experiments. The second section will discuss lepton universality and compare the results of this analysis with other recent results.

8.1 Branching Ratio

The $\tau^- \rightarrow e^- \bar{\nu}_e \nu_\tau$ branching fraction measured in this analysis is $B(\tau^- \rightarrow e^- \bar{\nu}_e \nu_\tau) = 0.1778 \pm 0.0009 \pm 0.0011$, where the first error is statistical and the second is systematic. Fig. 8.1 shows this value in comparison with previously published measurements of the $\tau^- \rightarrow e^- \bar{\nu}_e \nu_\tau$ branching ratio. The statistical and systematic errors are combined in quadrature for each of the branching ratio values. The vertical band in the figure indicates the error range of the average branching ratio from the Particle Data Group [7]. The Particle Data Group number is a weighted average of measurements up to 1994, all shown below the dashed line in Fig. 8.1. The result from this analysis agrees well with the Particle Data Group value of 0.1790 ± 0.0017 , and also with the recently published OPAL result based on 1990-1992 data.

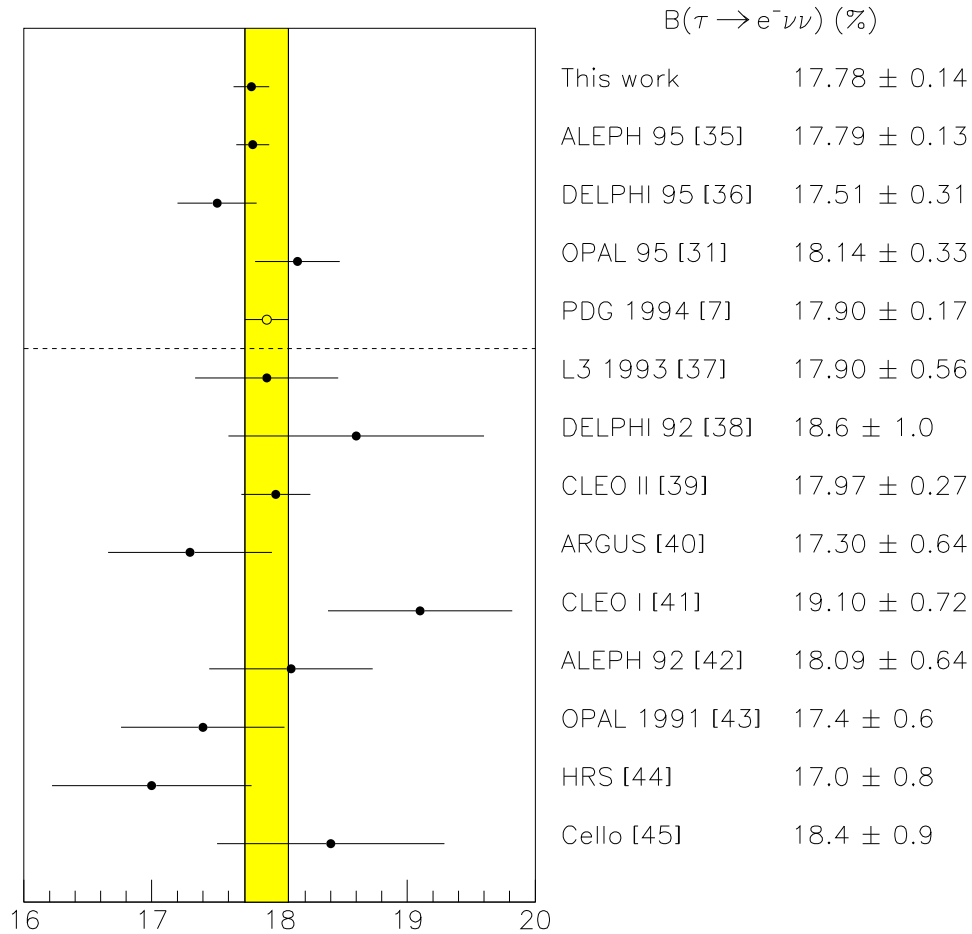


Figure 8.1: The electronic branching ratio of this work is compared to other recent measurements. The errors are the quadratic sum of the statistical and systematic errors. The band represents the error specified for the Particle Data Group $\tau^- \rightarrow e^- \bar{\nu}_e \nu_\tau$ branching ratio value. The Particle Data Group number is a weighted average of measurements up to 1994. Those measurements below the dashed line are included in the Particle Data Group number.

8.2 Lepton Universality

The results of this analysis allow one to directly test lepton universality. Electron-muon universality can be tested using equation (2.12). Using this equation and the OPAL $\tau^- \rightarrow \mu^- \bar{\nu}_\mu \nu_\tau$ branching ratio of 0.1736 ± 0.0027 [31] one obtains

$$\frac{g_e}{g_\mu} = 0.9981 \pm 0.0085,$$

where the statistical and systematic errors have been added in quadrature. This result supports the hypothesis of electron-muon universality. Fig. 8.2 displays g_e/g_μ for this analysis and compares it against results from other experiments. Electron-muon universality from the other tau-decay experiments was determined by entering the $\tau^- \rightarrow e^- \bar{\nu}_e \nu_\tau$ and $\tau^- \rightarrow \mu^- \bar{\nu}_\mu \nu_\tau$ branching ratio results from those experiments into equation (2.12). The ratio g_e/g_μ can also be measured by comparing the rates of the $\pi^- \rightarrow e^- \bar{\nu}_e$ and $\pi^- \rightarrow \mu^- \bar{\nu}_\mu$ decays, and also by using the $W^- \rightarrow e^- \bar{\nu}_e$ and $W^- \rightarrow \mu^- \bar{\nu}_\mu$ decays. One can see from the figure that the most precise tests of electron-muon universality have been made by measuring the pion leptonic branching ratios [47, 48].

Tau-muon universality can be tested using equation (2.14). Using the OPAL measurement of the tau lifetime $T_\tau = 288.8 \pm 2.2 \pm 1.4$ fs [46], the world average muon lifetime $T_\mu = 2.19704 \pm 0.00004$ μ s [7], and the $\tau^- \rightarrow e^- \bar{\nu}_e \nu_\tau$ branching ratio from this analysis one obtains

$$\frac{g_\tau}{g_\mu} = 1.0023 \pm 0.0058.$$

This result supports the hypothesis of tau-muon universality. As above, the statistical and systematic errors of the branching ratio have been combined in quadrature and then combined with the lifetime and mass uncertainties to estimate the final error. Fig. 8.3 displays g_τ/g_μ for this analysis and compares it to measurements from other experiments. The $\tau^- \rightarrow e^- \bar{\nu}_e \nu_\tau$ and $\tau^- \rightarrow \mu^- \bar{\nu}_\mu \nu_\tau$ branching ratio results from the other tau-decay experiments are entered into equation (2.14) for consistency. Note that g_τ/g_μ can also be tested by comparing the rates of the $W^- \rightarrow \tau^- \bar{\nu}_\tau$ and $W^- \rightarrow \mu^- \bar{\nu}_\mu$ decays.

The $\tau^- \rightarrow e^- \bar{\nu}_e \nu_\tau$ branching ratio from this analysis and the tau lifetime are displayed in Fig. 8.4. Also shown in this plot is the band representing the standard model relationship

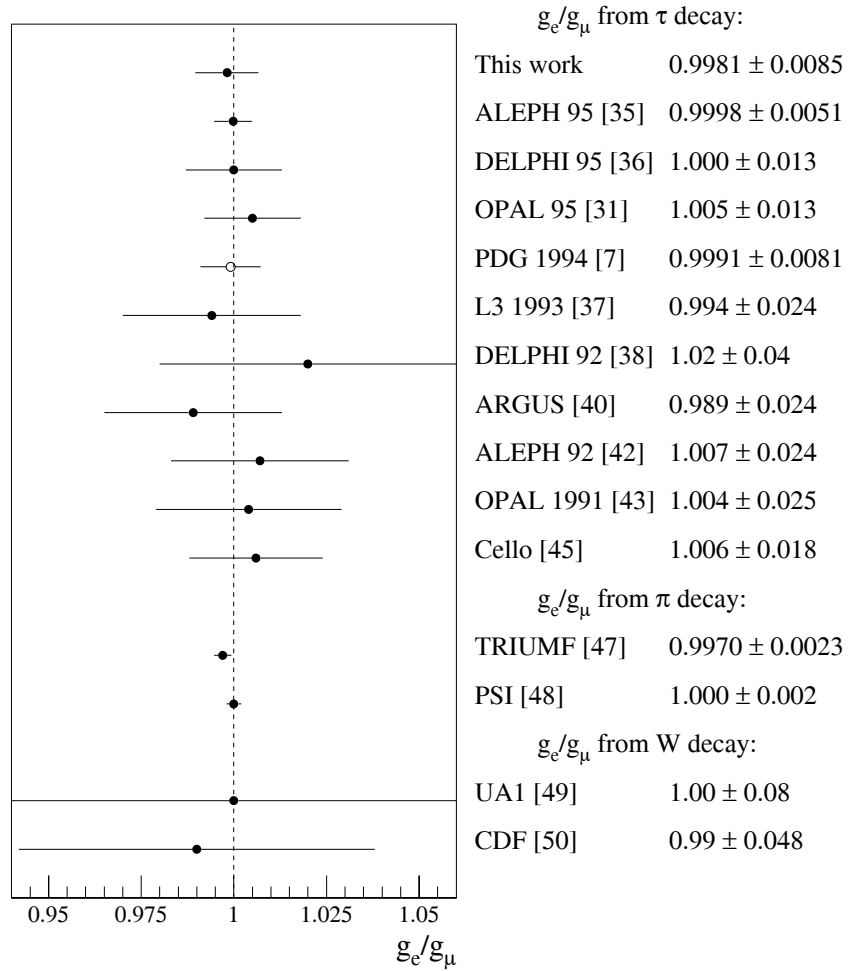


Figure 8.2: Electron-muon universality results of this work compared to other measurements. The pion and W decay results are taken directly from the references. The dotted line gives the value assuming electron-muon universality.

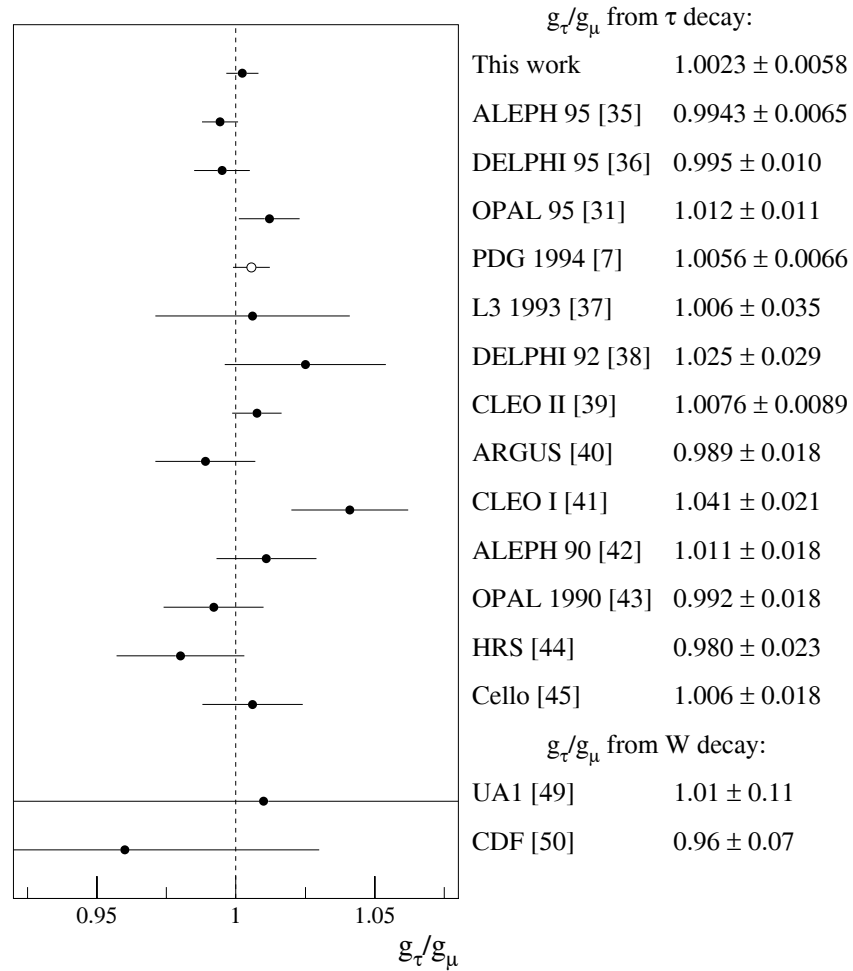


Figure 8.3: Tau-muon universality results of this work compared to other measurements. The results that use $B(\tau^- \rightarrow e^- \bar{\nu}_e \nu_\tau)$ are calculated using equation (2.14). The W decay results are taken directly from the references. The dotted line gives the value assuming tau-muon universality.

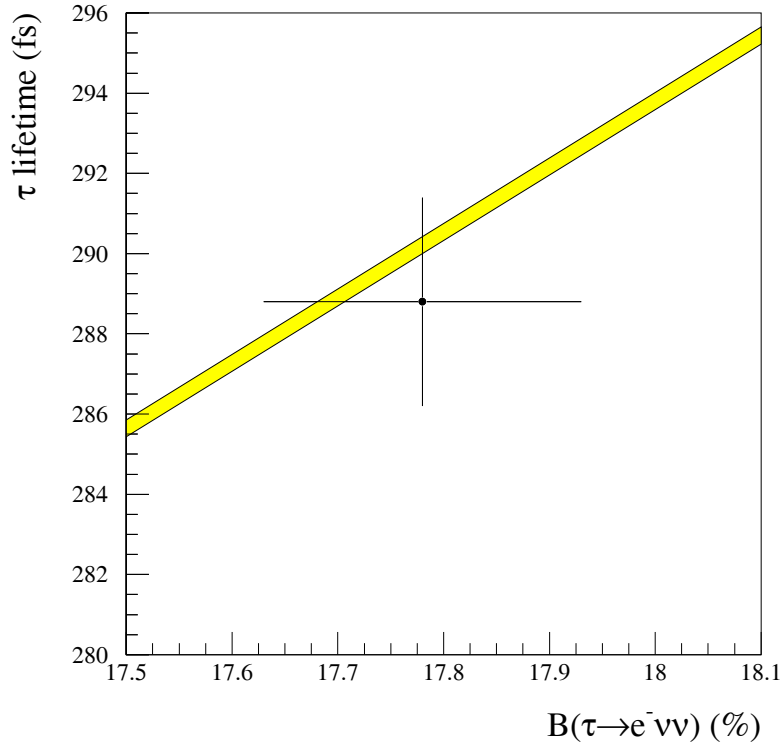


Figure 8.4: The OPAL lifetime measurement is plotted against the tau electronic branching ratio. The band displays the standard model relation between these quantities for a tau mass of $m_\tau = 1777.1^{+0.4}_{-0.5}$ MeV.

between these quantities (see eq. (2.14)), which is calculated assuming lepton universality. The small width of this band reflects the high precision of the tau mass measurement, since theoretical uncertainties on the prediction are negligible.

Chapter 9

Conclusion

The $\tau^- \rightarrow e^- \bar{\nu}_e \nu_\tau$ branching ratio was measured using data taken with the OPAL detector at LEP from 1991-1994 and has been determined to be

$$B(\tau^- \rightarrow e^- \bar{\nu}_e \nu_\tau) = 0.1778 \pm 0.0009 \pm 0.0011 ,$$

where the first error is statistical and the second is systematic. This result is the most precise determination to date and is consistent with previous measurements.

The $\tau^- \rightarrow e^- \bar{\nu}_e \nu_\tau$ branching ratio has been used together with other properties of the tau and also properties of the muon to test the principle of lepton universality. The ratio of the electroweak coupling constants, g_e/g_μ was determined to be 0.9981 ± 0.0085 , while the ratio g_τ/g_μ was determined to be 1.0023 ± 0.0058 . Together these results show consistency with the hypothesis of lepton universality to better than 1%.

Bibliography

- [1] J.C. Street and E.C. Stevenson, Phys. Rev. **52** (1937) 1003;
C.D. Anderson and S. Neddermeyer, Phys. Rev. **51** (1937) 884; **54** (1938) 88.
- [2] Perl, *et al.*, *Properties of Anomalous $e\mu$ Events Produced in e^-e^+ Annihilation*, Phys. Lett., **B 63** (1976) 466;
Feldman, *et al.*, *Inclusive Anomalous Muon Production in e^-e^+ Annihilation*, Phys. Rev. Lett., **B 38** (1977) 117 and 576.
- [3] W. Pauli, *Diracs Wellengleichung des Elektrons und geomtrische Optik*, Helv. Phys. Act. **5** (1932) 179.
- [4] F. Reines and C.L. Cowan, Jr., Phys. Rev. **92** (1953) 830.
- [5] H. Frauenfelder and E. Henley, *Subatomic Physics, Second Edition*, Prentice Hall, Englewood Cliffs, N.J., U.S.A., 1991.
- [6] F. Halzen and A. Martin, *Quarks and Leptons*, Wiley, 1984.
- [7] *Review of Particle Properties* Phys. Rev. **D 50** (1994).
- [8] S.L.Glashow, J.Hiopoulos and L.Maiani, Phys. Rev. **D 2** (1970) 1285;
S. Weinberg, Phys. Rev. Lett. **19** (1967) 1264;
A. Salam, *Elementary Particle Theory*, Ed. N. Svartholm, (Almquist and Wiksells, Stockholm, 1969) 357.
- [9] UA1 Collab., G. Arnison, *et al.*, Phys. Lett. **B 122** (1983) 103;
UA2 Collab., M. Banner, *et al.*, Phys. Lett. **B 122** (1983) 476.

- [10] B.C. Barish and R. Stroynowski, Phys. Rep. **157** (1988) 1.
- [11] Y. Tsai, Phys. Rev. **D 4** (1971) 2821.
- [12] T. Kinoshita and A. Sirlin, Phys. Rev. **113** (1959) 1652.
- [13] T.W. Appelquist, J.R. Primack and H.R. Quinn, Phys. Rev. **D 6** (1972) 2998;
T.W. Appelquist, J.R. Primack and H.R. Quinn, Phys. Rev. **D 7** (1973) 2998.
- [14] A. Sirlin, Rev. Mod. Phys. **50** (1978) 573.
- [15] W.J. Marciano, *Tau Physics - A Theoretical Perspective* Tau Workshop, Montreux, Switzerland, 1994
- [16] W.J. Marciano and A. Sirlin, Phys. Rev. Lett. **61** (1988) 1815.
- [17] LEP Design Report, CERN-LEP/TH/83-29 (1983).
- [18] The OPAL Collaboration, *The OPAL Detector at LEP*, Nucl. Inst. and Meth. **A 305** (1991) 275.
- [19] O. Biebel, *et. al.*, Nucl. Inst. and Meth. **A 323** (1992) 169.
- [20] U. Fano, Ann. Rev. Nucl. Sci. **13** (1963) 1.
- [21] A.H. Walenta, Physica Scripta **23** (1981) 354.
- [22] S. Kluth and D.R. Ward, *A Study of the Performance of the OPAL Electromagnetic Calorimeter using $e^+e^-\gamma$ Events*, OPAL Technical Note **TN108** (1992).
- [23] D. Lellouch, S. Weisz, *ROPE User's Guide*, OPAL-Offline note 16/OFFL-0487.
- [24] S. Jadach, B.F.L. Ward and Z. Was, Comp. Phys. Comm. **66** (1991) 276.
- [25] S. Jadach, J.H. Kühn and Z. Was, Comp. Phys. Comm. **64** (1991) 275.
- [26] J. Allison, *et. al.*, Nucl. Inst. and Meth. **A 317** (1992) 47.

- [27] R. Brun, F. Bruyant, M. Maise, A.C. M^cPherson and P. Zanolini, GEANT3, CERN-DD/EE/84-1 (1987).
- [28] OPAL Collaboration, G. Alexander, *et. al.*, Phys. Lett. **B 266** (1991) 201.
- [29] OPAL Collaboration, P. Acton, *et. al.*, Phys. Lett. **B 288** (1992) 373.
- [30] OPAL Collaboration, G. Alexander, *et. al.*, Z. Phys. **C 52** (1991) 175.
- [31] OPAL Collaboration, R. Akers, *et. al.*, Z. Phys. **C 66** (1995) 543.
- [32] OPAL Collaboration, R. Akers, *et. al.*, Phys. Lett. **B 328** (1994) 207.
- [33] OPAL Technical Note **TN285** (1995).
- [34] OPAL Technical Note **TN303** (1995).
- [35] ALEPH Collaboration, D. Buskulic, *et. al.*, CERN Preprint CERN-PPE/95-127.
- [36] DELPHI Collaboration, P. Abreu, *et. al.*, CERN Preprint CERN-PPE/95-114.
- [37] L3 Collaboration, O. Adriani, *et. al.*, Phys. Rep. **236** (1993) 1.
- [38] DELPHI Collaboration, P. Abreu, *et. al.*, Z. Phys. **C 55** (1992) 555.
- [39] CLEO Collaboration, D.S. Akerib, *et. al.*, Phys. Rev. Lett. **69** (1992) 3610;
CLEO Collaboration, D.S. Akerib, *et. al.*, Phys. Rev. Lett. **71** (1993) 3395.
- [40] ARGUS Collaboration, H. Albrecht, *et. al.*, Z. Phys. **C 53** (1992) 369.
- [41] CLEO Collaboration, R. Ammar, *et. al.*, Phys. Rev. **D 45** (1992) 3976.
- [42] ALEPH Collaboration, D. Decamp, *et. al.*, Z. Phys. **C 54** (1992) 211.
- [43] OPAL Collaboration, G. Alexander, *et. al.*, Phys. Lett. **B 266** (1991) 201.
- [44] HRS Collaboration, S. Abachi, *et. al.*, Phys. Rev. **D 41** (1990) 1414.
- [45] CELLO Collaboration, H.J. Behrend, *et. al.*, Z. Phys. **C 46** (1990) 537.

- [46] OPAL Collaboration, R. Akers, *et. al.*, Phys. Lett. **B 338** (1994) 497.
- [47] D.I. Britton, *et. al.*, Phys. Rev. Lett. **68** (1992) 3000;
D.I. Britton, *et. al.*, Phys. Rev. **D 49** (1994) 28.
- [48] G. Czapek, *et. al.*, Phys. Rev. Lett. **70** (1993) 17.
- [49] UA1 Collaboration, C. Aklbajar, *et. al.*, Z. Phys. **C 44** (1989) 15.
- [50] CDF Collaboration, F. Abe, *et. al.*, Phys. Rev. Lett. **69** (1992) 28.

VITA

Surname: LAWSON Given Names: IAN TIMOTHY
Place of Birth: Saint John, New Brunswick
Date of Birth: November 03, 1971

Educational Institutions Attended:

University of Victoria	1993 to 1995
University of New Brunswick	1989 to 1993

Degrees Awarded

B.Sc. (Honours) University of New Brunswick	1993
---------------------------------------------	------

Honours and Awards

Graduate Teaching Fellowship	1993/1994
Graduate Teaching Fellowship	1994/1995

PARTIAL COPYRIGHT LICENSE

I hereby grant the right to lend my thesis to users of the University of Victoria Library, and to make single copies only for such users or in response to a request from the Library of any other university, or similar institution, on its behalf or for one of its users. I further agree that permission for extensive copying of this thesis for scholarly purposes may be granted by me or a member of the University designated by me. It is understood that copying or publication of this thesis for financial gain shall not be allowed without my written permission.

Title of Thesis:

A Test of Lepton Universality
Using the $\tau^- \rightarrow e^- \bar{\nu}_e \nu_\tau$ Decay

Author: _____

Ian Timothy Lawson

November 29, 1995